# Evaluation of "on site" calibration procedures for sun-sky photometers

Monica Campanelli [1], Victor Estelles[2], Gaurav Kumar [2], Teruyuki Nakajima[3], Masahiro Momoi [4],
Julian Gröbner[5], Stelios Kazadzis[5], Natalia Kouremeti[5], Angelos Karanikolas[5], Africa Barreto[6],
Saulius Nevas[7], Kerstin Schwind[7], Philipp Schneider[7], Iiro Harju[8], Petri Kärhä[8], Henri Diémoz[9],
Rei Kudo[10], Akihiro Uchiyama[11], Akihiro Yamazaki[10], Anna Maria Iannarelli[12], Gabriele Mevi[12],
Annalisa Di Bernardino[13], Stefano Casadio[12].

1 Institute of Atmospheric Sciences and Climate , CNR, Rome, Italy
2 University of Valencia, Valencia, Spain
3 National Institute for Environmental Studies, 16–2 Onogawa, Tsukuba, Ibaraki 305-8506, Japan
4 GRASP SAS: Generalized Retrieval of Atmosphere and Surface Properties, Villeneuve d'Ascq, France.
5 Phys. and Meteo. Obs. Davos / World Radiation Center (PMOD/WRC), Davos, Switzerland
6Izaña Atmospheric Research Center (IARC), Agencia Estatal de Meteorología (AEMET), Santa Cruz de Tenerife,
Spain
7 Physikalisch-Technische Bundesanstalt (PTB), Braunschweig, Germany
8 Aalto University, Aalto, Finland
9 ARPA Valle d'Aosta, Saint Christophe, Italy
10 Meteorological Research Institute, Japan Meteorological Agency, Tsukuba, 305-0052, Japan
11 National Institute for Environmental Studies, Tsukuba, 305-0053, Japan
12 SERCO Italy, spa, Frascati, Italy.
13 Sapienza University of Rome, Department of Physics, Rome, Italy

**Corresponding author:** Monica Campanelli m.campanelli@isac.cnr.it

**Abstract**
To retrieve columnar aerosol properties from sun-photometers both irradiance and radiance calibration factors are needed.
For the irradiance the solar calibration constant, $V_0$, that is the instrument counts for a direct normal solar flux extrapolated
to the top of the atmosphere, must be determined. The solid view angle, SVA, is a measure of the field of view of the
instrument, and it is important for obtaining the Radiance from sky diffuse irradiance measurements. Each of the three
sun-photometers networks considered in the present study (SKYNET, AERONET, WMO-GAW) adopts different
protocols of calibration, and we evaluated the performance of the on-site calibration procedures, applied to SKYNET
PREDE-POM instruments, during intercomparison campaigns and laboratory calibrations held in the framework of the
Metrology for Aerosol Optical Properties (MAPP) EMPIR project. The on-site calibration, performed as frequently as
possible (rather monthly) to monitor change of the devise condition, allow operators to track and evaluate the calibration
status on a continuous basis considerably reducing the data gaps incurred by the periodical shipments for performing
centralized calibrations. The performance of the on-site calibration procedures for $V_0$ was very good in sites with low
turbidity, showing an agreement with a reference calibration between 0.5% and 1.5% depending on wavelengths. In the
urban area, the agreement decreases between 1.7% and 2.5%. For the SVA the difference varied from a minimum of
0.03% to a maximum of 3.46%.

## 1. Introduction

The ground-based remote sensing measurements of the solar radiation are an important part of atmospheric physics aimed
to determine the columnar aerosol optical properties. Sun-sky photometers and sun-photometers are instruments
performing direct and diffuse solar radiation measurements in the wavelength regions where gases' absorption is low or
negligible. Several networks have been established worldwide, such as AERONET (Holben et al., 1998), WMO-GAW
(Kazadzis et al., 2018a) and SKYNET (Nakajima et al., 2020). These networks provide well tracked, but with different
basic principles, calibration procedures, good quality standards and homogeneity on the retrievals. Traceability and data
quality are essential requirements by the World Meteorological Organization (WMO) for monitoring atmospheric aerosol
optical properties. In 2006, the Commission for Instruments and Methods of Observation (CIMO) of the WMO (WMO,
2007) recommended that the World optical depth research and calibration center (WORCC) at the PMOD-WRC is
designated as the primary WMO Reference Centre for aerosol optical depth (AOD) measurements (WMO, 2005). Since
2000, reference instruments from different networks are intercompared in order to ensure worldwide aerosol optical depth
homogeneity (e.g. Kazadzis et al., 2018b, Kim et al., 2008, WMO, 2023).
To obtain columnar aerosol properties from sun-photometers, both irradiance and radiance calibration factors are needed.
For the irradiance, the solar calibration constant ($V_0$) must be determined whereas the solid view angle (SVA) is an
intermediate step for the radiance calibration. $V_0$ is the instrument counts for a direct normal solar flux, F, (Irradiance,
instrument units) extrapolated to the top of the atmosphere (Shaw, 1976), and it is an important issue for the estimation

60  of the AOD. An error of 10% in the estimation of $V_0$ induces an uncertainty in the retrieval of AOD of about 0.1, therefore
61  a good accuracy is needed in its determination. SVA is a measure of the field of view of the instrument, and it is important
62  for obtaining the Radiance, L, ($Wm^{-1}sr^{-1}$) from sky diffuse irradiance measurements (E), being L the ratio between E and
63  SVA.
64  Each of the three networks considered in the present study adopts different protocols of calibration. For the AERONET
65  (Giles et al., 2019) CIMEL sun-sky photometers, $V_0$ is transferred from a value of reference instrument which is retrieved
66  by Langley-plot based on measurements at a mountaintop calibration site (Shaw, 1976; Holben et al., 1998). The primary
67  mountaintop calibration sites in AERONET are located at the Mauna Loa Observatory (latitude 19.536, longitude
68  −155.576, 3402 m) on the island of Big Island (Hawaii) and the Izana Observatory (latitude 28.309, longitude −16.499,
69  2401 m) on the island of Tenerife in the Canary Islands（Toledano et al., 2018, Cuevas et al., 2022). These reference
70  instruments are routinely monitored for stability and typically recalibrated every 3 to 8 months. Langley-calibrated
71  instruments move to main calibration locations (such as Washington DC (USA), the Observatoire de Haute-Provence
72  (OHP, France) or Valladolid (Spain)), and transfer their calibration to reference instrumentation. Then each of the CIMEL
73  network instruments are visiting these locations and they are calibrated. Radiance L is directly obtained by a calibration
74  with the integrating spheres at the AERONET calibration centers, providing an absolute calibration traceable to a NIST
75  standard lamp hosted at the NASA GSFC calibration facility.
76  WMO-GAW uses PFR sun-photometers measuring only the direct solar Irradiance. $V_0$ is calculated by comparison
77  against three Langley-calibrated instruments (triad) at the WORCC (Kazadzis et al., 2018a). The triad is also checked by
78  comparisons with instruments visiting WORCC every six months operating at Mauna Loa and Izana and perform Langley
79  calibrations. Within the ACTRIS European research infrastructure, three reference PFRs are permanently located at the
80  AERONET Europe calibration locations of OHP, Valladolid and Izana to ensure data homogeneity.
81  SKYNET adopts on-site calibration routines for the PREDE-POMs sun-sky photometers to determine the $V_0$ and SVA,
82  using the improved Langley plot method described in section 3.3 and the disk scan method (Nakajima et al., 1996; Boi et
83  al., 1999; Uchiyama et al., 2018) described in section 4.3. The on-site calibration procedures are performed as frequently
84  as possible (rather monthly) to monitor change of the device condition, since the deterioration of the optical filters or
85  other parts of the optics is detectable in a change of the temporal behavior of the calibration constants. On-site calibration
86  procedures allow operators to track and evaluate the calibration status on a continuous basis considerably reducing the
87  data gaps incurred by the periodical shipments for performing centralized calibrations. Also, the likelihood of instrumental
88  damages attributable to transport decreases.
89  In the present work we evaluate the performance of the on-site calibration procedures applied to two PREDE-POM
90  instruments, using intercomparison campaigns and laboratory calibrations held in the framework of the Metrology for
91  Aerosol Optical Properties (MAPP) EMPIR project. The overall aim of MAPP is to enable the SI-traceable measurement
92  of column-integrated aerosol optical properties retrieved from the passive remote sensing of the atmosphere using solar
93  and lunar radiation measurements.
94
95  **2.  Sites and instruments**
96  The on-site calibration procedures were applied to four different PREDE POMs of the SKYNET network (Table 1), using
97  datasets from the campaigns held in two mountain sites, Davos (9.846W, 46.814N, 1588.4 m a.s.l), and Izana (16.499E,
98  28.309N, 2373.0 m a.s.l), and in two urban sites, Rome (12.516W, 41.902N, 83.0, m a.s.l) and Valencia (0.418E,
99  39.508N, 60.0m a.s.l). The periods of the campaigns are also listed in Table 1:
100
101  Table1: List of the campaigns used for the evaluation of the on-site calibration procedure performance; * POM_CNR is
102  a Lunar and solar version.
103

| Campaign name | Location | Involved Instr. | Period |
|---|---|---|---|
| QUATRAM 1 | Davos | POM_VDV | 10/08/2017-31/08/2017 |
| QUATRAM 1 | Rome | POM_VDV | 22/09/2017-11/03/2017 |
| QUATRAM 2 | Davos | POM_22 | 24/07/2018-19/10/2018 |
| QUATRAM 2 | Rome | POM_22 | 01/05/2019-30/09/2019 |
| MAPP-QUATRAM 3 | Rome | POM_CNR * | 03/09/2021-20/09/2021 |
| FRC-QUATRAM 3 | Davos | POM_CNR* | 07/10/2021-19/10/2021 |
| MAPP Valencia | Valencia | POM_UV | 04/10/2022-30/11/2022 |
| MAPP Izana | Izana | POM_CNR* | 02/09/2022-22/09/2022 |

104
105  The QUAlity and TRaceabiliy of Atmospheric aerosol Measurements (QUATRAM) campaigns (Campanelli et al., 2018;
106  http://www.euroskyrad.net/quatram.html) are organized by the Institute of Atmospheric Science of CNR (Italy) and the
107  Physikalisch-Meteorologisches Observatorium Davos/World Radiation Center (PMOD/WRC). They are aimed to evaluate
108  the homogeneity and comparability among measurements performed by equipment of different International Networks
109  and/or manufactures, and to assess the accuracy of the new on-site calibration procedures. The Networks/Instruments
110  involved in QUATRAM are: SKYNET-PREDE/POM sun-sky photometers; AERONET-CIMEL 318 photometers;
111  WMO-Precision Filter Radiometer (PFR); Multi Filter Rotating Shadowband Radiometers (MFRSR) and Middleton
112  photometers. The approach consists of performing a calibration transfer from a primary master PFR of the PMOD/WRC

Atmospheric
Measurement
Techniques
Open Access

Discussions

EGU

113 to the other instrumentation, of the comparison of AODs at the common wavelengths, and of the evaluation of the on-site
114 calibration procedures. The campaigns were held in both urban (Rome) and mountain (Davos) sites to consider different
115 atmospheric turbidity and aerosol optical characteristics. The QUATRAM 3, held in Davos in 2021, was hosted by the
116 Fifth WMO Filter Radiometer Comparison (FRC-V) (WMO, 2023).
117 The Izana and Valencia campaigns were held in the framework of the Metrology for aerosol optical properties (MAPP)
118 project with the purpose of generating data to be used for a development of a comprehensive uncertainty budget for
119 aerosol optical properties from remote sensing techniques and to determine the Top-of-Atmosphere solar and lunar
120 spectra.
121 The evaluation of the performance of the SKYNET on-site calibration procedures was assessed by comparing the
122 retrieved constants against:
    a. the laboratory calibrations performed by the Physikalisch-Technische Bundesanstalt (PTB), Germany, the Aalto
       University, Finland, and the PMOD, Switzerland.
125     b. the transfer of calibration from PFR and CIMEL to PREDE-POM instruments operating simultaneously.
126 The PFR instrument, manufactured by PMOD/WRC, is used in the GAW AOD network, and it is a classic sun photometer
127 equipped with 3 to 5 nm bandwidth interference filters (368nm, 412 nm, 500 nm, 863 nm) and a field of view of 2.5∘.
128 The detector unit is held at a constant temperature of 20 ∘C by an active Peltier system. Dielectric interference filters
129 manufactured by the ion-assisted deposition technique are used to assure significantly larger stability in comparison to
130 manufactured by classic soft coatings. The PFR was designed for long-term stable measurements; therefore, the
131 instrument is hermetically sealed with an internal atmosphere that is slightly pressurized (2000 hPa) with dry nitrogen.
132 The CIMEL CE 318, standard AERONET instrument (Holben et al., 1998; Giles et al., 2019), is a multi-wavelength
133 automatic sun-sky photometer developed by Cimel Electronique, measuring direct solar irradiance and sky radiance at
134 nine bands (340 nm, 380 nm, 440 nm, 500 nm, 675 nm, 870 nm, 937 nm, 1020 nm, and 1640 nm) with 2-10 nm Full
135 Width at Half Maximum (FWHM) and a field of view of 1.3° (Torres et al., 2013). The detector is not thermostated and
136 corrections are performed a-posteriori. The PREDE-POM, standard instrument of the SKYNET network, is a sun-sky
137 photometer operating at seven wavelengths in the model 01 (315 nm, 400 nm, 500 nm, 675 nm, 870 nm, 940 nm, 1020
138 nm). Three of the four PREDE-POMs however have been modified by replacing the 315 nm filter with a filter at 340 nm.
139 The field of view is 1° and FWHM is equal to 3 nm (UV) and 10 nm (visible, VIS and near-infrared). The optics are
140 thermostated at 30°C.
141
142 **3. Estimation of the Solar calibration constant**
143 Six methods for the estimation of $V_0$ are analysed in the following sections: the in-lab calibration at PTB, the transfer of
144 calibration among instruments and the on-site procedures.
145
146 **3.1 The laboratory calibrations at PTB**
147 The two sun-sky radiometers, POM_UV and POM_CNR, were calibrated at PTB with respect to their spectral irradiance
148 responsivities. The calibrations were accomplished using the tunable laser-based facility, TUable Lasers In Photometry
149 (TULIP). The TULIP facility, shown in Figure 1, has recently been upgraded with a laser system based on an optical
150 parametric oscillator (OPO) operating in pulsed mode with a pulse length of 2.5 ps and a repetition rate of 80 MHz. The
151 laser wavelength is automatically tunable throughout the spectral range from 230 nm to 2300 nm. A high-accuracy laser
152 spectrum analyzer (LSA) is used to monitor the laser wavelength, which is stable within 10 pm during a typical
153 measurement sequence. The spectral bandwidth of the laser radiation is wavelength-dependent and varies between 0.2
154 nm and 0.7 nm in the visible spectral range. The centroid values of the measured laser spectrum are used as the
155 wavelengths of the corresponding spectral responsivity values.
156 A spatially homogeneous non-polarized field with temporally stabilized irradiance values is produced by a beam shaping
157 optics based on a micro lens array. The amplitude stabilization of the output radiation from the laser system is achieved
158 using two liquid crystal display (LCD)-based modulators inserted in the signal and idler beams of the OPO, before the
159 second and third harmonic (SHG and THG) modules of the laser system. The feedback signals for the control circuits of
160 the intensity modulators are taken from Si and InGaAs photodiodes irradiated by a fraction of the radiation field formed
161 by the micro lens array. In this way, the irradiance values at the measurement plane are stabilized to a level of a few parts
162 in $10^4$. The homogeneity of the generated field is within a few parts in $10^3$. Spectral irradiance responsivity calibrations
163 are made in such a field by comparing the signal of a device under test (DUT) to that of a reference detector (REF),
164 positioned sequentially at the same position in the measurement plane. The spectral irradiance responsivities of the
165 reference detectors built Si and InGaAs photodiodes for the visible and near infrared wavelengths, respectively, are
166 obtained through a chain of calibrations from a primary cryogenic radiometer and from the calibrated areas of the precision
167 radiometric apertures used with the reference detectors.
168 The spectral irradiance responsivity calibrations of the sun photometers were made at ca. 1.5 m from the micro lens array.
169 At this distance, the illuminated area of the micro lens array seen by the radiometers subtends ca 0.3 degrees. The entrance
170 apertures of the sun photometers were aligned perpendicular to the optical axis of the TULIP setup. The angular
171 orientation of the POM instruments in the setup was optimised by tilting and rotating to maximize the signal. This ensured
172 that the central part of the field of view was illuminated by the laser-induced irradiation field. The digital signals (DN)
173 from the POM instruments were requested and read via a serial port of the TULIP control PC using respective software
174 commands. During the measurements it was not possible to select the internal gain settings of the POMs. These settings

175 are managed by the instrument firmware. It was therefore also not possible to verify the gain values during the laboratory
176 calibrations and their respective contributions to the measurement uncertainties.
177
178

179
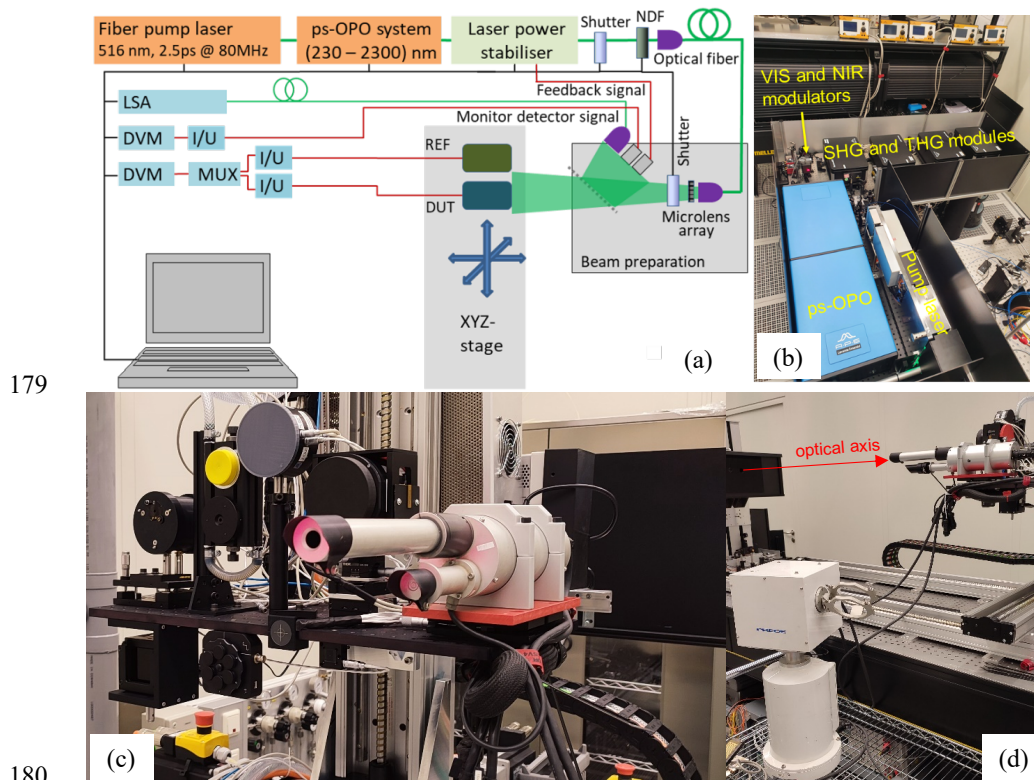

180
181
182
183 Figure 1. TULIP setup at PTB: (a) schematic representation of the setup including optical parametric oscillator (OPO)
184 system, variable neutral-density filter (NDF), reference (REF) and detector under test (DUT), current-to-voltage converter
185 (I/U), multiplexer (MUX), digital voltage meter (DVM) and laser spectrum analyzer (LSA); (b) a picture of the ps-OPO
186 system; (c) a picture of POM and reference detectors installed on the translation stage system; (d) a side view of the POM
187 facing the beam shaping optics inside the enclosure.
188
189
190 The results of the calibrations of all the channels of the two instruments are shown in Figure 2. The bandpass functions
191 of the spectral channels were found to match well the nominal filter function. Only the 940 nm channel of POM_UV
192 showed a large deviation. Most of the spectral channels were confirmed to block the out-of-band radiation to the level of
193 1E-8 throughout the whole spectral range.
194
195
196
197
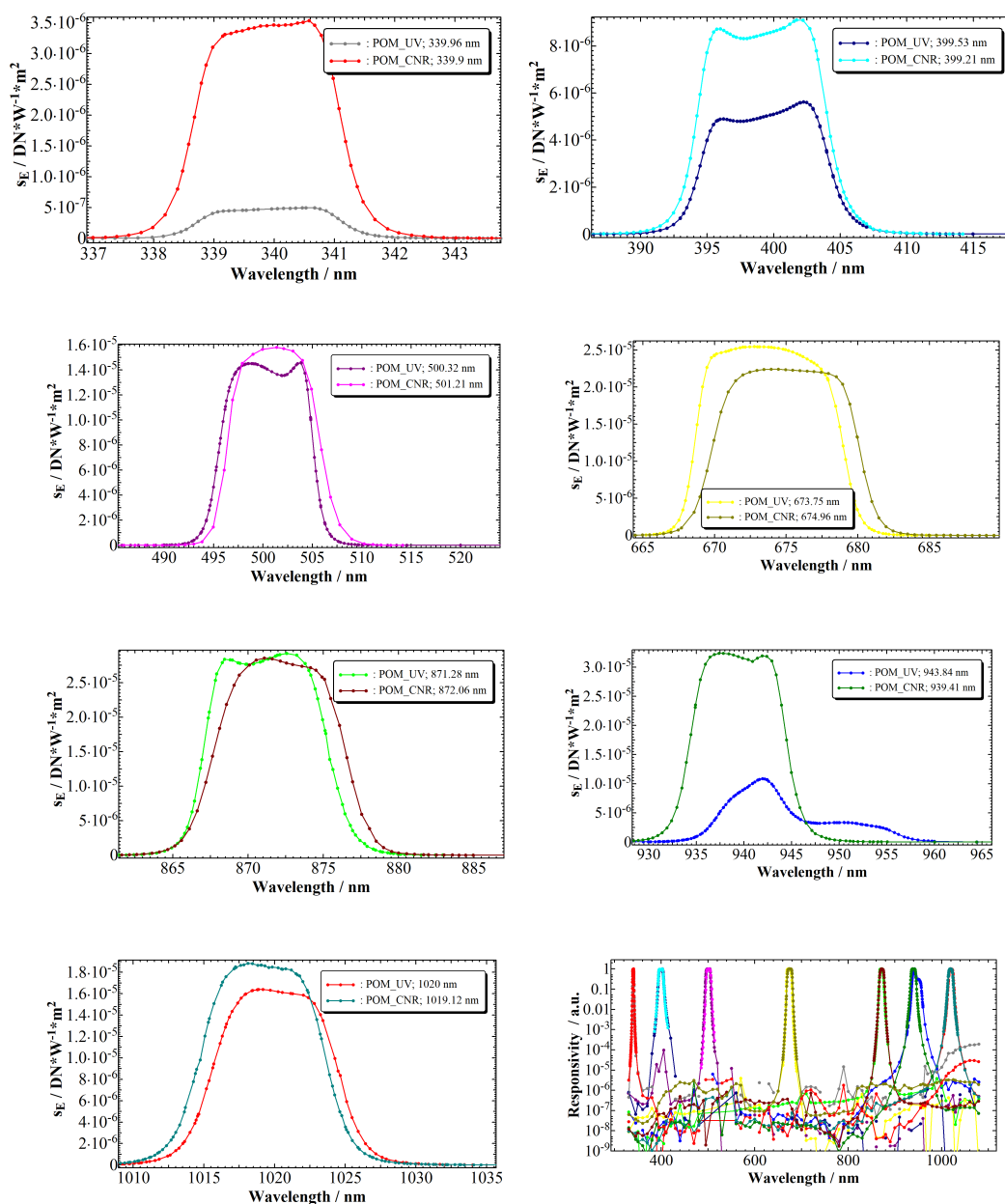
Figure 2. Measured spectral irradiance responsivities of all channels of the sun photometers and their normalized values displayed on a logarithmic scale.

The uncertainty analysis of the spectral irradiance measurements was accomplished by a Monte Carlo method according to Supplement 1 to the "Guide to the expression of uncertainty in measurement" using the measurement equation including all relevant uncertainty contributions. The know uncertainty components include the uncertainty of the reference detector responsivity, its aperture area, stability and LSA-based measurement of the laser wavelength, spatial homogeneity of the laser-generated field, the temporal stability of the irradiance values, laser bandwidth variation, and positioning of the detectors in the plane of measurements. For the latter uncertainty contribution, the position of the effective radiometric aperture of the measured detectors along the optical axis must be known. In the case of the reference

208  detectors with well-defined mechanical apertures, their position can be determined with an accuracy of better than 0.1
209  mm. However, the position of radiometrically limiting apertures of sun photometers with lens optics cannot be measured
210  directly as they are behind the lens. In this case, they were determined through distance variation with much higher
211  resulting uncertainties. For the Prede POM sun photometers, the positions of the effective apertures could be determined
212  with estimated standard uncertainties of 3 mm. The respective uncertainty contribution was also dominating the
213  uncertainty of the spectral irradiance responsivity calibrations of the filter radiometers (Figure 3).
214  It should be noted that the uncertainty analysis only included the uncertainty components identified during the laboratory
215  calibrations under the respective measurement conditions. As mentioned above, uncertainty contributions from internal
216  gain values of the POMs could not be estimated due to the lack of functionality of the instruments for laboratory
217  calibrations. Also, the temperature stabilization of the POM_CNR did not work during the calibrations at PTB. The effect
218  of the instrument malfunction on the calibrated responsivity values was not included in the uncertainty analysis. In
219  addition, there may be some other differences between the operating conditions of the instruments during the laboratory
220  calibrations and their use in the field, which could lead to additional uncertainty contributions.
221
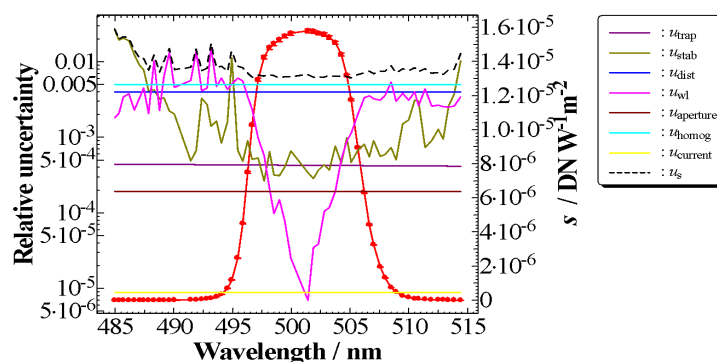


223  Figure 3. Example of spectrally dependent uncertainty components of spectral irradiance responsivity measurements of
224  the 500 nm channel of POM_CNR. The relative uncertainties on the left axis represent components due to reference
225  detector ($u_{trap}$), temporal irradiance stability ($u_{stab}$), detector positioning ($u_{dist}$), laser wavelength ($u_{wl}$), REF aperture area
226  ($u_{aperture}$), spatial homogeneity ($u_{homog}$), photocurrent measurements of REF ($u_{current}$), and the resulting standard uncertainty
227  of the measurements ($u_s$).

230  The calibration factors $V_0$ were obtained a posteriori, by integration of the spectral response and the extra-terrestrial TSIS
231  spectrum (Coddington et al., 2023). The uncertainties were estimated by quadratic error propagation of the numerical
232  integral. The results are summarised in Table 2.

234  Within the EMPIR project 19ENV04 MAPP, sun photometers from GAW-PFR and AERONET networks  were also
235  measured at PTB with respect to their spectral irradiance responsivities. The results of the laser-based calibrations of
236  several sun photometers were verified by additional methodologies for laboratory calibrations. The spectral irradiance
237  responsivities of a PFR and two CIMELs determined at the TULIP setup were verified by a calibration against reference
238  standard lamps with traceability to the primary spectral irradiance standard (a high-temperature blackbody). The results
239  agreed well within the uncertainties of the calibrations, i.e. in the range between 0,2%  and 1%. One CIMEL was also
240  calibrated in radiance mode using an integrating sphere source calibrated at PTB for the spectral radiance. This calibration
241  data combined with the FOV values measured by PMOD yielded spectral irradiance responsivities of the CIMEL channels
242  that agreed within 1% to 2% to those determined at the TULIP setup in irradiance mode.
243  The spectral irradiance responsivities of the PRF were combined with the published spectral irradiance at the top of the
244  atmosphere (TOA) values (QASUMEFTS ($\lambda \leq 500$) & TSIS-1 HSRS ($\lambda > 500$ nm)) to derive the signal values that would
245  be measured at the TOA. Those values were compared with those obtained by the Langley technique. The agreement
246  between the values was within 0,5%. Also the AOD values derived using the laboratory-based calibration of the PFR
247  were well in agreement to those from the Langley-based calibration (Kouremeti et al, 2021; Gröbner et al., 2023).
248  For the three CIMEL instruments calibrated at PTB, the agreement between the calculated TOA values and those derived
249  by the Langley extrapolation technique was in the range of 1% to 5%, with the discrepancies systematically increasing
250  towards the short-wavelength channels. Thus, for all instruments, the results of the in-lab calibrations were consistent
251  within their respective uncertainties, regardless of the calibration methods used.

**3.2   The standard Langley (SL) method for POM_CNR**
254  The Standard Langley method (Shaw, 1976) is the most common procedure adopted to calculate the solar calibration
255  constant. It is based on the Beer-Lambert law (Eq. 1)

256

$$V = V_0 \, exp \, (-m_0 \tau)$$
$$\text{Or}$$
$$ln \, V = ln \, V_0 - m_0 (\tau_{gas} + \tau_R) - m_0 \tau_{ext}$$

Eq.1

257
258 Where V is the direct solar irradiance measured at ground, $m_0$ is the optical air mass as the inverse of the cosine of the
259 solar zenith angle, $\tau_{ext}$ is the extinction AOD, $\tau_{gas}$ and $\tau_R$ are are respectively the gas absorption optical depth and the
260 molecular (Rayleigh) scattering optical depth.
261 The Standard Langley method consists of the retrieval of $V_0$ by the fit of y vs x in Eq. 2, assuming that optical depth due
262 to aerosol is constant, as it happens performing the measurements at high altitude (i.e. above the boundary layer, where
263 AOD is low and its absolute variability is also very low).

$$y = a_{SL} + b_{SL} x \quad where$$
$$x = m_0$$
$$y = ln \, V + m_0 \cdot (\tau_{gas} + \tau_R)$$

Eq.2

264
265 The linear fitting provides intercept $a_{SL} = ln \, V_0$ and slope $b_{SL} = -\tau$.
266 This method is used for measurements taken at the Izaña observatory by the POM_CNR. The following criteria are used
267 to filter the data: i) only data for $m_0 \geq 2$ and $\leq 5$ are considered; ii) using $a$ and $b$ parameters retrieved from the fit, $y_{fit}$ is
268 obtained from Eq.2 and the residuals are calculated for each point as $y - y_{fit}$; their RMSD is calculated and if it is $> 0.006$,
269 the mean of residuals is calculated and points for which residual is greater than mean value are removed; a new fit is then
270 performed and the process is repeated until RMSD $< 0.006$ is obtained; iii) special criterion is applied for 340 nm where
271 data points were only selected for m $< 2$. The primary reason for choosing this airmass threshold is its sensitivity towards
272 molecules (Rayleigh scattering). Selecting higher optical mass means light gets scattered more and can cause errors. A
273 similar strategy is also used in Estelles, et al. (2004). The selected series were considered only if the number of data points
274 are greater than 50. After a visual inspection, three days of the Izana campaign (7, 8 and 9 September, 2022) were very
275 stable and showed minor fluctuations. Calibration values were calculated for these three days, both in the morning (before
276 13 UTC) and afternoon for each wavelength with the air mass limit between 2 and 5.
277 Uncertainty was determined as the standard deviation of the calibration values calculated for three days in morning and
278 evening (6 plots). The mean was taken as the final calibration value. Results are shown in Table 2a and b.
279

Atmospheric
Measurement
Techniques

Open Access

Discussions

| Location | yymm | Type | POM_CNR V0_IL*e-04 (A) | | | | | | %CV | | | | | | Unc. | | | | | |
|---|---|---|---|---|---|---|---|---|---|---|---|---|---|---|---|---|---|---|---|---|
| | | | 340 | 400 | 500 | 675 | 870 | 1020 | 340 | 400 | 500 | 675 | 870 | 1020 | 340 | 400 | 500 | 675 | 870 | 1020 |
| Davos | 1708 | IL | | 1.363 | 2.828 | 3.486 | 2.229 | 1.164 | | 2.63 | 1.87 | 1.24 | 1.04 | 1.28 | | | 5.2884E-06 | 4.3226E-06 | 2.3182E-0 | 1.4899E-06 |
| | | XIL | | 1.3411 | 2.8384 | 3.5466 | 2.2336 | 1.1984 | | 4.06 | 2.41 | 3.05 | 1.75 | 4.32 | | 5.4430E-06 | 6.8334E-06 | 1.0821E-05 | 3.8981E-06 | 5.1719E-06 |
| | | PFR | | | 2.844 | | 2.231 | | | | 0.22 | | 0.27 | | | | 6.126E-07 | | 5.933E-07 | |
| Rome | 1710 | IL | | 1.307 | 2.782 | 3.454 | 2.204 | 1.151 | | 2.2 | 1.29 | 0.71 | 0.85 | 1.48 | | 2.8754E-06 | 3.5888E-06 | 2.4523E-06 | 1.8734E-06 | 1.7035E-06 |
| | | XIL | | 1.3101 | 2.7803 | 3.4634 | 2.2171 | 1.1417 | | 6.05 | 2.16 | 1.31 | 0.81 | 1.16 | | 7.9275E-06 | 6.0121E-06 | 4.5426E-06 | 1.7925E-06 | 1.3215E-06 |
| | | PFR | | | 2.858 | | 2.226 | | | | 0.11 | | 0.19 | | | | 3.043E-07 | | 4.266E-07 | |
| Davos | 1807 | IL | 0.0886 | 1.289 | 2.751 | 3.268 | 2.3 | 1.236 | 0.77 | 0.71 | 0.35 | 0.19 | 0.36 | 1.01 | 6.8245E-08 | 9.1519E-07 | 9.6285E-07 | 6.2092E-07 | 8.28E-07 | 1.2484E-06 |
| | | XIL | 0.0896 | 1.3061 | 2.7756 | 3.284 | 2.3203 | | 1.65 | 1.53 | 1.25 | 0.73 | 0.68 | | 1.4809E-07 | 2.0023E-06 | 3.4809E-06 | 2.3990E-06 | 1.5773E-06 | |
| | | PFR | | | 2.781 | | 2.325 | | | | 0.25 | | 0.18 | | | | 6.948E-07 | | 4.221E-07 | |
| Davos | 1808 | IL | 0.0888 | 1.3 | 2.762 | 3.294 | 2.321 | 1.228 | 1.4 | 1.3 | 0.97 | 0.85 | 0.97 | 0.52 | 1.2438E-07 | 1.6900E-06 | 2.6791E-06 | 2.7999E-06 | 2.2514E-06 | 6.3856E-07 |
| | | XIL | 0.0889 | 1.3045 | 2.788 | 3.3126 | 2.3282 | 1.2396 | 3.35 | 2.84 | 2.24 | 1.29 | 0.87 | 0.86 | 2.9799E-07 | 3.7027E-06 | 6.2579E-06 | 4.2749E-06 | 2.0167E-06 | 1.0606E-06 |
| | | PFR | | | 2.799 | | 2.349 | | | | 0.50 | | 0.94 | | | | 1.410E-0 | | 2.204E-06 | |
| Davos | 1809 | IL | 0.0888 | 1.298 | 2.771 | 3.312 | 2.343 | 1.24 | 1.37 | 0.74 | 0.41 | 0.18 | 0.2 | 0.6 | 1.217E-07 | 9.6052E-07 | 1.1361E-06 | 5.9616E-07 | 4.686E-07 | 7.44E-07 |
| | | XIL | 0.0897 | 1.3065 | 2.7897 | 3.3606 | 2.3744 | 1.2379 | 3.42 | 1.68 | 1.52 | 2.17 | 1.18 | 0.50 | 3.0721E-07 | 2.1913E-06 | 4.2431E-06 | 7.2794E-06 | 2.7935E-06 | 6.2217E-07 |
| | | PFR | | | 2.801 | | 2.368 | | | | 0.19 | | 0.43 | | | | 5.387E-07 | | 1.017E-06 | |
| Davos | 1810 | IL | 0.0881 | 1.286 | 2.766 | 3.317 | 2.346 | 1.259 | 0.73 | 0.53 | 0.31 | 0.1 | 0.36 | 0.84 | 6.4298E-08 | 6.8158E-07 | 8.5746E-07 | 3.317E-07 | 8.4456E-07 | 1.0576E-06 |
| | | XIL | 0.0892 | 1.3025 | 2.7791 | 3.3306 | 2.3561 | | 1.01 | 1.09 | 0.54 | 0.42 | 0.24 | | 8.9976E-08 | 1.4159E-06 | 1.4910E-06 | 1.3825E-06 | 5.7300E-07 | |
| | | PFR | | | 2.802 | | 2.364 | | | | 0.14 | | 0.17 | | | | 3.842E-07 | | 3.991E-07 | |
| Rome | 1905 | IL | 0.0857 | 1.274 | 2.717 | 3.268 | 2.321 | 1.235 | 1.23 | 1.1 | 0.55 | 0.54 | 1.81 | 1.17 | 1.0542E-07 | 1.4014E-06 | 1.4944E-06 | 1.7647E-06 | 4.201E-06 | 1.445E-06 |
| | | XIL | 0.0877 | 1.3061 | 2.7466 | 3.2535 | 2.2858 | 1.2063 | 3.13 | 4.75 | 1.32 | 2.29 | 3.48 | 2.23 | 2.7478E-07 | 6.2097E-06 | 3.6318E-06 | 7.4567E-06 | 7.9489E-06 | 2.6940E-06 |
| | | PFR | | | 2.804 | | 2.348 | | | | 0.55 | | 0.55 | | | | 1.552E-06 | | 1.280E-06 | |
| Rome | 1906 | IL | 0.0852 | 1.269 | 2.73 | 3.272 | 2.303 | 1.228 | 0.51 | 0.66 | 0.72 | 0.69 | 0.7 | 0.48 | 4.3467E-08 | 8.3754E-07 | 1.9656E-06 | 2.2577E-06 | 1.6121E-06 | 5.8944E-07 |
| | | XIL | 0.0865 | 1.2875 | 2.7762 | 3.3197 | 2.3329 | 1.2497 | 4.56 | 2.15 | 2.17 | 2.33 | 2.00 | 2.64 | 3.9447E-07 | 2.7702E-06 | 6.0374E-06 | 7.7213E-06 | 4.6677E-06 | 3.3028E-06 |
| | | PFR | | | 2.809 | | 2.347 | | | | 0.68 | | 0.49 | | | | 1.909E-06 | | 1.144E-06 | |
| Rome | 1907 | IL | 0.0841 | 1.261 | 2.737 | 3.257 | 2.299 | 1.231 | 1.67 | 1.61 | 1.07 | 0.47 | 0.37 | 0.26 | 1.4043E-07 | 2.0302E-06 | 2.9286E-06 | 1.5308E-06 | 8.5063E-07 | 3.2006E-07 |
| | | XIL | 0.0859 | 1.2938 | 2.7704 | 3.3159 | 2.3329 | 1.246 | 3.06 | 2.83 | 1.68 | 1.71 | 1.25 | 0.99 | 2.6246E-07 | 3.6563E-06 | 4.6446E-06 | 5.6785E-06 | 2.9061E-06 | 1.2319E-06 |
| | | PFR | | | 2.836 | | 2.366 | | | | 0.21 | | 0.17 | | | | 5.946E-07 | | 3.893E-07 | |
| Rome | 1908 | IL | 0.0847 | 1.278 | 2.765 | 3.324 | 2.329 | 1.25 | 0.93 | 0.68 | 0.4 | 0.22 | 0.18 | 0.34 | 7.8752E-08 | 8.6904E-07 | 1.106E-06 | 7.3128E-07 | 4.1922E-07 | 4.25E-07 |
| | | XIL | 0.0862 | 1.298 | 2.7833 | 3.3328 | 2.3305 | 1.25 | 2.98 | 3.34 | 1.52 | 1.37 | 0.96 | 1.11 | 2.5662E-07 | 4.3291E-06 | 4.2278E-06 | 4.5499E-06 | 2.2329E-06 | 1.3820E-06 |
| | | PFR | | | 2.834 | | 2.369 | | | | 0.55 | | 0.25 | | | | 1.559E-06 | | 5.794E-07 | |

| Site | Period | Method | $V_0$ (6 channels) | | | | | | CV % (6 channels) | | | | | | Unc (6 channels) | | | | | |
|---|---|---|---|---|---|---|---|---|---|---|---|---|---|---|---|---|---|---|---|---|
| Rome | 1909 | IL | 0.0841 | 1.26 | 2.747 | 3.315 | 2.32 | 1.246 | 2.34 | 1.63 | 0.96 | 0.62 | 0.47 | 0.43 | 1.9675E-07 | 2.0538E-06 | 2.637E-06 | 2.055E-06 | 1.0904E-06 | 5.3578E-07 |
|  |  | XIL | 0.0866 | 1.309 | 2.823 | 3.3463 | 2.3356 | 1.2564 | 3.94 | 3.61 | 2.87 | 1.90 | 1.11 | 0.95 | 3.4160E-07 | 4.7260E-06 | 8.0981E-06 | 6.3714E-06 | 2.5963E-06 | 1.1914E-06 |
|  |  | PFR |  |  | 2.838 |  | 2.369 |  |  |  | 0.12 |  | 0.07 |  |  |  | 3.260E-07 |  | 1.754E-07 |  |
| Rome | 2108 | IL |  | 1.251 | 2.716 | 3.301 | 2.259 | 1.266 |  | 2.61 | 2.47 | 2.61 | 0.28 | 0.91 |  | 3.3402E-06 | 6.709E-06 | 8.616E-06 | 6.3252E-07 | 3.9246E-07 |
|  |  | XIL | 0.0854 | 1.2788 | 2.7291 | 3.2931 | 2.2788 | 1.2458 | 2.75 | 3.25 | 2.46 | 1.65 | 1.48 | 0.39 | 2.3456E-07 | 4.1561E-06 | 6.7215E-06 | 5.4234E-06 | 3.3797E-06 | 1.1382E-06 |
| Rome | 2109 | IL | 0.0818 | 1.232 | 2.686 | 3.268 | 2.25 | 1.25 | 2.17 | 2.73 | 2.29 | 2.87 | 2.99 | 2.50 | 1.006E-03 | 1.663E-02 | 1.638E-02 | 1.699E-02 | 1.215E-02 | 4.875E-03 |
|  |  | XIL | 0.083 | 1.251 | 2.7016 | 3.2964 | 2.2847 | 1.2526 | 1.23 | 1.35 | 0.61 | 0.52 | 0.54 | 0.39 | 1.8048E-07 | 3.4187E-06 | 6.1926E-06 | 9.4722E-06 | 6.8267E-06 | 3.1340E-06 |
|  |  | PFR |  |  | 2.754 |  | 2.302 |  |  |  | 0.22 |  | 0.44 |  |  |  | 6.179E-07 |  | 1.004E-06 |  |
|  |  | Cim_1270 | 0.085 |  |  |  |  |  | 1.48 |  | 1.10 | 1.09 | 1.10 | 1.49 | 1.250E-07 |  | 3.020E-06 | 3.600E-06 | 2.510E-06 | 1.830E-06 |
| Davos | 2110 | IL | 0.0851 | 1.255 | 2.698 | 3.271 | 2.293 | 1.219 | 1.41 | 0.51 | 0.22 | 0.11 | 0.2 | 0.61 | 1.200E-03 | 6.401E-03 | 5.936E-03 | 3.598E-03 | 4.586E-03 | 7.436E-03 |
|  |  | XIL | 0.0862 | 1.2612 | 2.7043 | 3.2928 | 2.302 |  | 0.53 | 0.86 | 0.63 | 0.00 | 0.31 |  | 4.5824E-08 | 1.0882E-06 | 1.7002E-06 |  | 7.2490E-07 |  |
|  |  | PFR |  |  | 2.734 |  | 2.311 |  |  |  | 0.13 |  | 0.20 |  |  |  | 3.628E-07 |  | 4.713E-07 |  |
| PTB | 2206 | Lab | 0.0903 | 1.3225 | 2.9680 | 3.5506 | 2.4146 | 1.2473 | 4.4 | 4.3 | 4.2 | 4.2 | 4.1 | 4.2 | 4.000E-07 | 5.700E-06 | 1.300E-05 | 1.500E-05 | 1.000E-05 | 5.300E-06 |
| Izana | 2209 | SL | 0.0855 | 1.2551 | 2.6982 | 3.2715 | 2.2965 | 1.2372 | 2.53 | 1.09 | 0.40 | 0.15 | 0.45 | 0.66 | 2.160E-07 | 1.370E-06 | 1.090E-06 | 5.070E-07 | 1.040E-06 | 8.210E-07 |

Table 2a: Solar calibration constants $V_0$, percent Coefficients of variation CV, and uncertainties calculated as described from sections 3.1-3.6, for all the methods and periods, for POM_CNR. When CV or Unc is 0, the monthly dataset is composed by only one point. In column three, there is the type of method used: IL (Improved Langley), XIL (Cross Improved Langley), PFR (Transfer from PFR instrument), Cim_1270 (Transfer from Cimel), Lab (laboratory calibration), SL (Standard Langley).

281

Atmospheric Measurement Techniques
Open Access
Discussions

| Site | Year | Method | V0_IL*e-04 (A) | | | | | | %CV | | | | | | Unc | | | | | |
|---|---|---|---|---|---|---|---|---|---|---|---|---|---|---|---|---|---|---|---|---|
| | | | 340 | 400 | 500 | 675 | 870 | 1020 | 340 | 400 | 500 | 675 | 870 | 1020 | 340 | 400 | 500 | 675 | 870 | 1020 |
| Rome | 2109 | IL | 0.0118 | 0.7635 | 2.535 | 3.803 | 2.266 | 1.084 | 2.87 | 2.32 | 0.63 | 0.54 | 0.45 | 0.70 | 3.3859E-08 | 1.7683E-06 | 1.6029E-06 | 2.0540E-06 | 1.0129E-06 | 7.5869E-07 |
| Rome | 2109 | Cim_1270 | 0.0124 | | 2.6149 | 3.8487 | 2.3072 | 1.0580 | 1.19 | | 1.18 | 1.05 | 1.07 | 1.43 | 1.477E-08 | | 3.082E-06 | 4.037E-06 | 2.471E-06 | 1.516E-06 |
| Rome | 2109 | PFR | | | 2.6153 | | 2.3130 | | | | 1.38 | | 1.12 | | | | 3.6159E-06 | | 2.5904E-06 | |
| PTB | 2206 | Lab | 0.0123 | 0.7893 | 2.7770 | 3.9341 | 2.3583 | 1.0889 | 4.4 | 4.2 | 4.2 | 4.1 | 4.1 | 4.2 | 5.430E-08 | 3.280E-06 | 1.180E-05 | 1.610E-05 | 9.770E-06 | 4.520E-06 |
| Valen. | 2210 | IL | 0.0116 | 0.761 | 2.565 | 3.841 | 2.287 | 1.081 | 1.04 | 0.66 | 0.97 | 1.37 | 1.23 | 1.86 | 1.2027E-08 | 5.0584E-07 | 2.4780E-06 | 5.2583E-06 | 2.8130E-06 | 2.0128E-06 |
| Valen. | 2210 | XIL | 0.0117 | 0.7633 | 2.6103 | 3.8144 | 2.2878 | 1.0986 | 3.55 | 7.41 | 6.71 | 2.73 | 2.06 | 7.00 | 4.1569E-08 | 5.6586E-06 | 1.7509E-05 | 1.0429E-05 | 4.7225E-06 | 7.6943E-06 |
| Valen. | 2211 | IL | 0.0123 | 0.7804 | | 3.873 | 2.32 | 1.081 | 1.61 | 2.05 | | 0.54 | 0.66 | 1.67 | 1.9807E-08 | 1.5959E-06 | | 2.0918E-06 | 1.5219E-06 | 1.8031E-06 |
| Valen. | 2211 | XIL | 0.0122 | 0.7841 | 2.6006 | 3.8652 | 2.3123 | 1.0574 | 1.22 | 0.00 | 0.17 | 0.38 | 0.48 | 0.00 | 1.4838E-08 | 0.00 | 4.4522E-07 | 1.4502E-06 | 1.1173E-06 | 0.00 |
| Valen/ Izaña | 2211 | SL_tranf | 0.0124 | 0.7776 | 2.5673 | 3.8002 | 2.3105 | 1.0753 | 2.58 | 1.11 | 0.44 | 0.26 | 0.50 | 0.73 | 3.2100E-08 | 8.6415E-07 | 1.1423E-06 | 9.9221E-07 | 1.1599E-06 | 7.8000E-07 |

Table 2b: Solar calibration constants V0, percent Coefficients of variation CV, and uncertainties calculated as described from sections 3.1-3.6, for all the methods and periods, for POM_UV. When CV or Unc is 0, the monthly dataset is composed by only one point. In column three, there is the type of method used: IL (Improved Langley), XIL (Cross Improved Langley), PFR (Transfer from PFR instrument),Cim_1270 (Transfer from Cimel), Lab (laboratory calibration), SL_trans (Transfer from POM_CNR Standard Langley).

Atmospheric
Measurement
Techniques
Discussions

283
284 ### 3.3 The improved Langley methods (IL-XIL) for POM_CNR and POM_UV
285 Based on the above-described Langley method, the formula of Improved Langley method is expressed as follows:
286

$$y = a_{IL} + b_{IL}x \quad where$$
$$x = m_0\omega\tau_{ext} = m_0\frac{\tau_{sca}}{\tau_{ext}}\tau_{ext} = m_0\tau_{sca} \; and$$
$$y = ln\, V + m_0 \cdot (\tau_{gas} + \tau_R) \qquad \qquad \text{Eq.3}$$

287
288 where ω is the aerosol single scattering albedo (defined as $\frac{\tau_{sca}}{\tau_{ext}}$). The linear fitting provides intercept $a_{IL} = ln\, V_0$ and slope
289 $b_{IL} = -\frac{1}{\omega}$.
290 The improved Langley plot method (Campanelli et al., 2004 and 2007, Nakajima et al., 2020) is the standard calibration
291 method of the SKYNET network and it was used to calculate the solar calibration constants for both the Prede-POM sun-
292 sky photometers.
293 The calibration value, $V_0$, is retrieved by fitting the natural logarithm of the direct solar irradiance versus the product of
294 $m_0$ and the scattering optical depth, as retrieved by the SKYRAD 4.2 code (Nakajima et al., 2020), instead of only the air
295 mass as occurs with the standard Langley plot.
296
297 To understand the main idea on which this method is based, we define the two observable quantities (for each wavelength
298 λ) important for the Sun-sky photometer, the direct solar irradiance in Eq. 1 and the normalized radiance R in Eq. 4
299

$$R(\Theta) = \frac{E(\Theta)}{\Delta\Omega \cdot V \cdot m_0} \qquad \qquad \text{Eq. 4}$$

300 where $\Theta$ is the scattering angle at which the Prede-POM takes measurements of the sky diffuse irradiance $E$, V is direct
301 irradiance and $\Delta\Omega$ is the solid-view angle of the instrument.
302
303 R is determined as the solution of the radiative transfer equation, as in Eq.5 in the Almucantar geometry for a one-layer
304 plane-parallel atmosphere, where P is the phase function, and q indicates the multiple-scattering contribution
305

$$R(\Theta) = \omega\tau_{ext}P(\Theta) + q(\Theta) = \tau_{sca}P(\Theta) + q(\Theta) \qquad \qquad \text{Eq. 5}$$

306

307 Thus, normalized radiance R is approximately assumed as the product of $\tau_{sca}$ and P; $\tau_{sca}$ is derived via the inversion process
308 (e.g., Skyrad 4.2) of volume size distribution from the normalized radiance in aureole region with scattering angles 3° <
309 $\Theta$ < 30° (Nakajima et al., 2020), keeping fixed the refractive index, and it is used in the improved Langley method for
310 obtaining the intercept $V_0$. Note that the aerosol optical depth for scattering (in $x$ in Eq. 3) is potentially retrieved more
311 accurately than the optical depth for extinction $\tau_{ext}$. To understand the reason, it must be considered that the volume size
312 distribution is roughly obtained by only direct radiation information because of the limited information content of the
313 extinction Kernel function (Tonna et al., 1995, Figure 4). On the other hand, for the sky radiance measurements in the
314 range 3° < $\Theta$ < 30°, the scattering kernel functions (Tonna et al., 1995, Figure 4) have reliable information content
315 (approximately within $1 < 2\pi r/\lambda < 60$, which means that $0.05 < r < 10$ μm for our wavelength set) that is sufficient for
316 deriving volume size distribution and reliably reconstructing the connected quantities R, P, $\omega\tau_{ext}$. The radiance in the
317 aureole region is also less sensitive to the refractive index (Tanaka et al., 1983), Therefore, the use of R in Eq.5 to obtain
318 $\omega\tau_{ext}$, i.e. scattering optical thickness, is the best way to analyze data. In contrast to the standard Langley method, the
319 intercept $V_0$ does not depend on the daily variability of $\omega\tau_{ext}$ if the inversion process is accurate.

320 From R and V data collected each month, two $V_0$ values a day are calculated with data taken in the morning and in the
321 afternoon, and the $V_0$ monthly means are quality checked according to Campanelli et al., 2007, and below summarized:
322 i) the values of $\omega\tau_{ext}$ obtained from the SKYRAD4.2 code inversion with accuracy lower than 7% are rejected. The
323 accuracy is estimated as the percent differences between the measured and retrieved radiance R, averaged over all the
324 wavelengths and scattering angles; ii) only the measurements taken for $m_0 < 3.0$ and $1/\omega > 0$ and $\leq 2$ are selected; iii) all
325 the values of $V_0$ found for $\tau_{ext}$ (500 nm) $\geq 0.4$ are rejected; iv) a minimum number of 10 points is used in each morning
326 and afternoon fit.
327 The rejection of $\tau_{ext}$ (500 nm) values greater than 0.4, is not in contradiction with the AERONET strategy, where the
328 retrieval of ω is performed only for $\tau_{ext} > 0.4$ (Aeronet web page, Holben et al., 2006) otherwise ω and other properties
329 are not included in the L2 analysis, because the purpose of this selection for IL is different. Infact a potential problem in
330 this procedure is that the refractive index is kept fixed. The aureole region has information for volume size distribution,
331 but not for refractive index, as said before, and this allows to retrieve $\tau_{sca}$. However, high $\tau_{ext}$ makes high multiple
332 scattering contribution ($q(\Theta)$ in Eq. 5) and greater error in retrieving $\tau_{sca}$ with a fixed refractive index.
333

Atmospheric
Measurement
Techniques
Open Access
Discussions
EGU

334 Once the filtered monthly $V_0$ series are obtained, the outliers and short-term variations related to the method itself are
335 filtered using the Chauvenet criterion (H. D. Young, 1962), that rejects points out of 2 times the standard deviation (std),
336 and a three-point moving average technique. Finally, if at least 3 values remain and the ratio between their std and mean
337 (Coefficient of variation, CV) is <3%, the monthly mean $V_0$ value is calculated. The uncertainty related to this value is
338 given for each wavelength by the CV coefficient. Results are shown in Table 2.

339

340 In the real observations, it is difficult to separate natural variations and inversion errors of $\omega\tau_{ext}$ and thus undesired
341 inversion errors can be included that lead the IL method to an underestimation of the fitting parameters in the case of
342 large aerosol retrieval errors (Nakajima et al., 2020). A new solution to this problem is tested, named the cross IL method
343 (XIL), which exchanges the role of x and y in the regression analysis as described in Eq. 6

344

$$x = a_{XIL} + b_{XIL}y \qquad \text{Eq. 6}$$

345 The linear fitting provides slope $b_{XIL} = \frac{1}{b_{IL}} = -\omega$ and intercept $a_{XIL} = -\frac{a_{IL}}{b_{IL}} = \omega ln V_0$

346

347 The selection of data for this method is performed using the threshold of 0.05 for the fitting error, assuming that
348 retrieval errors on $\omega$ and $\tau$ from Skyrad are within 9% (Nakajima et al., 2020). Monthly $V_0$ and the corresponding %CV
349 are then calculated. Results are shown in Table 2.

350

351 ### 3.4 The standard Langley method Transfer from POM_CNR to POM_UV
352 The calibration of the Prede POM_CNR by the Standard Langley Plot method at Izaña campaign in September 2022, was
353 transferred to POM_UV using data from the QUATRAM3 campaign, on September 2021, as it was the only campaign
354 where both instruments were co-located.
355 After visual inspection of the signal ratios for the days of September 2021, the days in the intervals 4-9, 11-15, 17-19, are
356 considered for the calibration transfer.
357 The transfer procedure consisted of the following steps: i) data were selected between 9 to 13 UTC; ii) signals within 30
358 sec between POM_UV and POM_CNR were considered; iii) $V_0$ for POM_UV was calculated following Eq. 7:

359
360

$$V_0^{POM\_UV} = V_0^{POM\_CNR} \cdot \frac{V^{POM\_UV}}{V^{POM\_CNR}} \qquad \text{Eq.7}$$

361 iv) values that are more than three scaled median absolute deviations away from the median are assumed as outliers and
362 deleted; v) daily $V_0^{POM\_UV}$ medians are calculated and 2std of the $V_0^{POM\_UV}$ series is calculated. If 2std is larger than 0.5%
363 of the daily $V_0$ median, all data outside 2std are removed. The process is repeated until 2std becomes equal or smaller
364 than 0.5% of the daily $V_0^{POM\_UV}$ median or standard deviation and median values becomes equal in continuous iteration;
365 vi) after visual inspection only days were selected which are stable, resulting in the exclusion of the days stated before.
366 To calculate the uncertainty of the transferred calibration values, the equation below was used, where we account for
367 uncertainties on the master instrument calibration, and the standard deviation of the signal ratios, that are sensitive to
368 changes in AOD, etc.

369

$$u(V_0^{POM\_UV}) = V_0^{POM\_UV} \cdot \sqrt{\left(\frac{u(V_0^{POM\_CNR})}{V_0^{POM\_CNR}}\right)^2 + \left(\frac{STD(SR)}{SR}\right)^2} \qquad \text{Eq.8}$$

370 where: $V_0^{POM\_UV}$ is the mean of the calibration values series and $u(V_0^{POM\_UV})$ is the uncertainty associated; $V_0^{POM\_CNR}$ is
371 the calibration factor, and $u(V_0^{POM\_CNR})$ is the uncertainty associated with it. This uncertainty was estimated as the
372 standard deviation of the 6 calibration values obtained by the 6 plots used in section 3.2; $SR$ is the ratio of signals
373 $\left(\frac{V^{POM\_UV}}{V^{POM\_CNR}}\right)$ and $STD(SR)$ is the standard deviation of the ratio of the signals available for the calibration. Results are in
374 Table 2.

375

376 ### 3.5 The calibration transfer from PFR to POM_CNR and POM_UV
377 The transfer of calibration from two reference PFR photometers of the PMOD one located in Davos and the other in
378 Rome, has been carried out for both POM_CNR and POM_UV, during the QUATRAM campaigns.
379 The transfer is based on the ratio of Eq. 9 for the two instruments, POM and PFR:
380

$$\frac{V_0^{POM,TR}}{V_0^{PFR}} = \frac{V^{PFR}}{V^{POM}} \qquad \text{Eq.9}$$

Atmospheric
Measurement
Techniques
Discussions
Open Access
EGU

381  where, V$^{\text{PFR}}$ and V$^{\text{POM}}$ are the solar direct irradiance measured by the two instruments, $V_0^{POM,TR}$ is the unknown solar
382  calibration constant of the POM and $V_0^{PFR}$ the known calibration constant of the PFR to be transferred. For QUATRAM
383  3 in Rome, days in the intervals (6-8; 11-14) of September 2021 were considered.

384  Signals ratios $\frac{V^{PFR}}{V^{POM}}$ were taken using measurements that are within 30 sec time difference, and cloudy conditions were
385  removed, together with ratios outliers. Values out of the interval time 9-13 UTC were rejected. The time interval was
386  chosen as 9-13 to avoid the rapid change in airmass. From Eq.9 the time series of $V_0^{POM,TR}$ was limited to: i) choosing
387  only those days for which at least 20 measurements in 1 hour are available; ii) Calculating the daily $V_0$ medians and
388  compare each with 2std of the day's $V_0$ values; if 2std is larger than 0.5% of the daily $V_0$ median, remove all data outside
389  2std; repeat until 2std becomes equal or smaller than 0.5% of the daily $V_0$ median; when this is accomplished, if the day's
390  measurements have dropped below 20 the day is excluded. Daily medians of the remaining values are calculated, and
391  then a monthly mean $V_0^{POM,TR}$ is estimated. As uncertainty the std of the monthly mean values is assumed. Results are in
392  Table 2.
393  For the transfer to POM_UV during QUATRAM 3, the same procedure was applied but the selected days are in intervals
394  (6-9; 11-14) of September 2021.
395  The uncertainties were estimated as in other transfer cases, by assuming a nominal uncertainty of the PFR calibration of
396  1%. Results for both instruments are in Table 2.
397  The same procedure was applied for the QUATRAM 3 in Davos and QUATRAM 1 and 2 in both the sites for POM_CNR.
398
399  **3.6  Calibration transfer from CIMEL to POM_CNR and POM_UV**
400  During QUATRAM 3, a calibration transfer from the Cimel #1270 was carried on, following the same selection criteria
401  of the transfer from PFR.
402  To calculate the total uncertainty of the transferred calibration values, Eq. 8 was used with $V_0^{CIM}$ as the master instrument
403  and $u(V_0^{CIM})$ the associated uncertainty. As the estimated uncertainty is absent for the master instrument, it is assumed to
404  nominal 1% of $V_0$. Results are in Table 2.
405
406  **3.7  Comparisons**
407
408    *a)  Differences between all methods against the reference one*

409  The six calibration methods described in the above sections in the period September 2021- November 2022 for both the
410  POMs are compared against a reference calibration. The time interval was chosen because the campaigns and laboratory
411  calibrations were performed in this period in the framework of the MAPP project.
412  For the POM_CNR the reference calibration is the Standard Langley method performed at Izana in September 2022,
413  whereas the transfer of this calibration to the POM_UV is the reference value for the latter instrument. However, we need
414  to consider that the frequent shipments of the equipment during this year for the project purpose and the usage can have
415  affected the values of $V_0$ and probably can be the reason of discrepancies between the SL calibration and the calibrations
416  performed about 1 year earlier. The aging of the instrument, without shipments, can also affect the $V_0$ but the order of
417  magnitude and amount per year strongly depends on the instrument, and some wavelengths can be more affected than
418  others. For the two instruments used in this work it is not possible to evaluate a degradation in one year and discern it
419  from the shipment's effects, because the equipment was frequently travelling.
420  The percent difference was calculated with Eq.10:
421

422  $$Diff(\%) = \frac{(V_0^{ref} - V_0^x)}{V_0^{ref}} \cdot 100 \qquad \text{Eq. 10}$$

423  where V$_0$$^{\text{ref}}$ is the reference value and V$_0$$^{\text{x}}$ is the calibration obtained with each of the above-described methods. Results
424  are shown in Figure 4 and Table 3.
425  For the POM_CNR the agreement is very good with the reference SL and many of the points are within ±1%.
426  The agreement generally improves with the wavelengths but with a small worsening at 1020 nm. The transfer from Cimel
427  and PFR in Rome and from PFR in Davos at 500 nm differ of -1.6%, -2.1% and -1.3%, respectively. 340 nm is the
428  wavelength with the most problematic results for the on-site procedures in Rome (differences around 4%). Further studies,
429  not yet published, showed that the 340 nm is also significantly affected by the assumed surface Albedo, and improvements
430  of the agreement were found if, for example, values from the POLarization and Directionality of the Earth's Reflectances
431  radiometer (POLDER) on ADEOS satellite, are considered. More tests are neede to verify this dependence in for more
432  sites. Moreover, according to Momoi (2022) the molecular polarization potentially causes calibration errors from IL and
433  XIL methods at the UV region (340 nm), especially low aerosol loading atmosphere. In fact the SKYRAD.pack 4.2 used
434  for the on-site procedures has an un-polarized ("scalar") radiative transfer core forward model, that can cause around 8%
435  errors on the retrieval of radiance at 340 nm, so it might be one of the reasons for the calibration constant of 340 nm to
436  have errors.
437  The best agreement is for the IL in Davos with values < 0.5% at all the wl, and 1.5% at 1020 nm.
438  For the POM_UV, many points are within ±1% but less respect to the POM_CNR. The agreement with the reference
439  method for the PTB laboratory calibration shows an improvement, remaining however between -1.3% and -8% except

440 for the 340 nm where it is 0.7%. Also for the POM_UV, an improvement with the wavelengths is notable with a worsening
441 at 1020 nm. The transfer from Cimel and PFR in Rome at 500 nm agrees within -1.9 %, a value comparable with those
442 of the POM_CNR. Also, in this case the 340 nm is the wavelength with the most problematic results for the on-site
443 procedures (differences up to 6%) as explained for the POM_CNR.
444 For both POMs, the comparison with PTB calibration shows very high underestimations (down to -10% except for
445 POM_CNR, and -8% for POM_UV), but at this state of the art we are not able to provide a certain reason for the
446 discrepancy. It is noteworthy that the agreement between the laboratory calibration and the Langley measurements for
447 PFR was well consistent within the uncertainties. In the case of the CIMELs, however, discrepancies increasing towards
448 the short wavelengths and exceeding the uncertainties by a factor of 2-3 have been observed. The causes of the
449 discrepancies between the laboratory calibrations and the field measurements of the CIMEL and POM instruments are
450 not yet understood. The instruments are obviously aligned and operated using different procedures when calibrated in the
451 laboratory and when measuring in the field. CIMEL and especially POM have narrower field of views than the PFR,
452 which makes them more susceptible to alignment and tracking errors, which could possibly lead to systematic
453 underestimation of the measured irradiance values. It should be noted that the comparison results shown in Figure 4 are
454 all from relative (Langley) measurements, with the exception of those based on the absolute responsivity calibrations at
455 PTB, which makes the respective result in the comparison particularly sensitive to the effects mentioned above.
456 Focusing on the on-site methodologies, the IL works better in Davos with an agreement against SL always below 0.5%
457 except at 1020 nm where it increases up to about 1.5%. A very good accordance is also found in Valencia in November
458 2022, always within 0.8% except at 500 and 675 nm (within 1.5%). The similarity between the two cases is probably due
459 to the very low turbidity recorded in this month in Valencia, that makes the atmosphere optically more similar to the one
460 in Davos.
461 The XIL provides a consistent improvement, with values within 1%, only in Rome for all the wavelengths, but in very
462 clean atmosphere, as in Davos, it was not possible to retrieve values at 1020 nm, as conversely is done with the IL. This
463 is related to the differences in the data screening criteria between the two methods, set up for performing the linear fitting.
464

465



466
467
468 Figure 4. The percent coefficients of variation, calculated as the % ratio between the standard deviation and the mean
469 values.
470
471

472    Table 3.  % Differences between five calibration methods and the reference one and % CV of the retrieved V$_0$.
473

| | | POM_CNR | % difference | | | | | | % CV | | | | | |
|---|---|---|---|---|---|---|---|---|---|---|---|---|---|---|
| | | | 340 | 400 | 500 | 675 | 870 | 1020 | 340 | 400 | 500 | 675 | 870 | 1020 |
| Rome | 2109 | IL | 4.29 | 1.84 | 0.45 | 0.11 | 2.02 | -1.04 | 1.23 | 1.35 | 0.61 | 0.52 | 0.54 | 0.39 |
| Rome | 2109 | XIL | 2.91 | 0.32 | -0.13 | -0.76 | 0.51 | -1.25 | 2.17 | 2.73 | 2.29 | 2.87 | 2.99 | 2.17 |
| Rome | 2109 | PFR | | | -2.08 | | -0.25 | | | | 0.22 | | 0.44 | |
| Rome | 2109 | Cim_1270 | 1.39 | | -1.55 | -1.18 | 0.28 | 0.58 | 1.48 | | 1.10 | 1.09 | 1.10 | 1.49 |
| Davos | 2110 | PFR | | | -1.33 | | -0.63 | | | | 0.13 | | 0.20 | |
| Davos | 2110 | IL | 0.42 | 0.00 | 0.01 | 0.02 | 0.15 | 1.47 | 1.41 | 0.51 | 0.22 | 0.11 | 0.20 | 0.61 |
| Davos | 2110 | XIL | -0.83 | -0.49 | -0.23 | -0.65 | -0.24 | | 0.53 | 0.86 | 0.63 | 0.00 | 0.31 | |
| PTB | 2206 | | -5.58 | -5.37 | -10.00 | -8.53 | -5.14 | -0.82 | 4.4 | 4.3 | 4.2 | 4.2 | 4.1 | 4.2 |
| | | POM_UV | 340 | 400 | 500 | 675 | 870 | 1020 | 340 | 400 | 500 | 675 | 870 | 1020 |
| Rome | 2109 | IL | 4.82 | 1.81 | 1.26 | -0.07 | 1.93 | -0.81 | 2.87 | 2.32 | 0.63 | 0.54 | 0.45 | 0.70 |
| Rome | 2109 | Cim_1270 | -0.04 | | -1.86 | -1.27 | 0.14 | 1.61 | 1.19 | | 1.18 | 1.05 | 1.07 | 1.43 |
| Rome | 2109 | PFR | | | -1.87 | | -0.11 | | | | | | | |
| PTB | | | 0.74 | -1.50 | -8.17 | -3.52 | -2.07 | -1.26 | 4.4 | 4.2 | 4.2 | 4.1 | 4.1 | 4.2 |
| Valencia | 2210 | IL | 6.35 | 2.14 | 0.09 | -1.07 | 1.02 | -0.53 | 1.04 | 0.66 | 0.97 | 1.37 | 1.23 | 1.86 |
| Valencia | 2210 | XIL | 5.71 | 1.84 | -1.68 | -0.37 | 0.98 | -2.16 | 3.55 | 7.41 | 6.71 | 2.73 | 2.06 | 7.00 |
| Valencia | 2211 | IL | 0.79 | -0.36 | | -1.91 | -0.41 | -1.16 | 2.05 | | 0.54 | 0.66 | 1.67 | 2.05 |
| Valencia | 2211 | XIL | 1.68 | -0.84 | -1.30 | -1.71 | -0.08 | 1.05 | 1.22 | | 0.17 | 0.38 | 0.48 | |

474
475        *a)   Long term differences between on-site calibrations and PFR transfer*

476    The difference between the on-site calibration methods and the PFR calibration transfer was analyzed in the period of the
477    3 QUATRAM campaigns held in Davos and Rome using Eq.10 with $V_0^{ref}$ the transfer from PFR. V$_0$s are shown in Table
478    2 and the percent difference is in Table 4 and Figure 5.
479
480
481
482    Table 4. % Differences between PFR transfer of calibration and the on-site calibration methods at the common
483    wavelengths.

| | | | % diff 500 nm | | % diff 870 nm | |
|---|---|---|---|---|---|---|
| | | Date | IL | XIL | IL | XIL |
| DAVOS | | 1708 | 0.56 | 0.20 | 0.09 | -0.12 |
| | | 1807 | 1.08 | 0.19 | 1.08 | 0.20 |
| | | 1808 | 1.32 | 0.39 | 1.19 | 0.89 |
| | | 1809 | 1.28 | 0.62 | 1.06 | -0.27 |
| | | 1810 | 1.28 | 0.82 | 0.76 | 0.33 |
| | | 2110 | 1.32 | 1.09 | 0.78 | 0.39 |
| ROME | | 1710 | 2.66 | 2.72 | 0.99 | 0.40 |
| | | 1905 | 3.10 | 2.05 | 1.15 | 2.65 |
| | | 1906 | 2.81 | 1.17 | 1.87 | 0.60 |
| | | 1907 | 3.49 | 2.31 | 2.83 | 1.40 |
| | | 1908 | 2.43 | 1.79 | 1.69 | 1.63 |
| | | 1909 | 3.21 | 0.53 | 2.07 | 1.41 |
| | | 2109 | 2.47 | 1.90 | 2.26 | 0.75 |

484
485
486

Atmospheric
Measurement
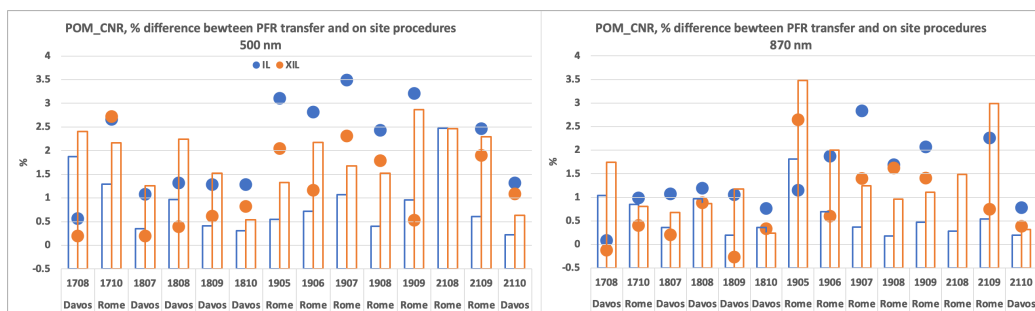Techniques

Open Access

Discussions



487
488
489    Figure 5. Percent differences between PFR transfer of calibration and the on-site calibration methods at the common
490    wavelengths (circles), and the uncertainty %CV of the IL and XIL as in Table 2.
491
492    For the IL, the differences are always greater than the uncertainties (%CV) of the method, for both wavelengths, with the
493    exception of Davos in 2017. Values are around 1% in Davos and this is an important result for the validation of the IL
494    procedure, confirming the good performance of the Improved Langley on high mountain even if, as shown in Nakajima
495    et al. (2020), the IL accuracy is proportional to the optical thickness of the atmosphere of observation, generally low on
496    high mountains. The same result has been also obtained by Ningombam et al. (2014). The largest differences are in Rome
497    and at 500 nm, although the higher AOD as shown in Figure 6. The reason could be related to the fact that in the retrieval
498    of $x$ for performing the fit in Eq.3, $\omega\tau_{ext}=\tau_{sca}$ and the refractive index must be assumed to not largely change during the
499    Langley plot (Campanelli et al., 2004), otherwise the retrieved optical thickness can include an error caused by the
500    inversion process and also by an improper pre-assigning of the refractive index. In an urban site, as Rome, we can expect
501    this assumption not satisfied. Further studies are actually aimed to understand the possibility of defining some selection
502    criteria for the variability of $\tau_{sca}$ values particularly in urban sites. Moreover the use of the Skyrad_MRI (Kudo et
503    al.,2021) instead of Skyrad 4.2 and possibility to use only the XIL method instead of the IL, is underevaluation.
504    For XIL many differences are within the uncertainties (%CV) of the method, and those higher are closer to the %CV
505    values than in the IL method. XIL improves the agreement particularly in Rome where the largest difference reduces from
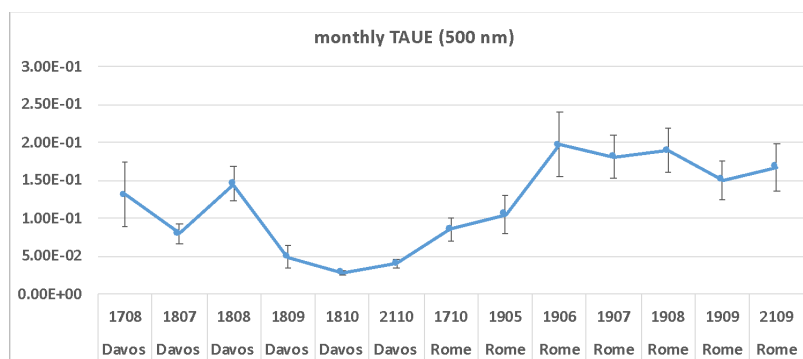506    3.5% to 2.5% at 500 nm and from 3% to 1.7% at 870 nm.
507
508



509
510    Figure 6. Monthly average and std of $\tau_{ext}$ at 500 nm from POMs listed in Table1.
511
512
513
514    **4.  Estimation of the solid view angle (SVA)**
515    The SVA is the measure of the field of view of the instrument that can be assumed from the geometry of the telescope.
516    However, several factors contribute to this value: color aberration of the lens, diffraction at the edges, misalignment of
517    the optical axis, and surface nonuniformity of filters and sensor. This makes it necessary to develop laboratory and on-
518    site methods for correctly estimating SVA values.  The methods used in this work are described below.
519
520    **4.1  Calibration at the laboratory of the AALTO University**
521    The field of view of the Prede POM_CNR has been measured at the laboratory of  Aalto University. The measurement
522    setup consists of a two-axis gimbal and a light source. The light source is constructed from an integrating sphere
523    (Gigahertz Optik type UMBB-300) and a 1 kW Xe-lamp. The diameter of the sphere is 300 mm, and the output aperture

16

524 is limited to 10 mm in diameter. The distance $D$ between the sphere aperture and the axis of rotation was $\approx 1060$ mm
525 (Figure 7). The purpose of the integrating sphere is to obtain a spatially uniform, well-defined light source. The aperture
526 size and the distance $D$ chosen provide the radiometer to see the light source at a solid angle corresponding to the same
527 solid angle where it sees the Sun in the field measurements, angular diameter = 0.54˚.
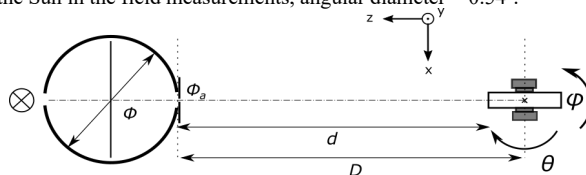


528

529 Figure 7: Schematic of the measurement setup. From left to right: a switchable light source, an integrating
530 sphere, and a two-axis gimbal.

531

532 The radiometer is mounted on the gimbal, tilted in the desired angle, and the signal amplitude is measured. The setup is
533 built on an optical rail, which enables easy varying of the distance between the gimbal and the light source. The light
534 source and gimbal are fixed in place. The point of rotation of the radiometer was chosen using an $x$-axis translator, and
535 customized elevation blocks installed between the radiometer and the gimbal to set $y$-direction. The common optical axis
536 of the light source and the radiometer is found by shifting the sphere aperture. The tilt angle range of measurements is [-
537 0.7˚ 0.8˚] for all channels in both directions, and the step size is 0.1˚. The measurement sequence and the data collection
538 are automated using LabView. The integrating sphere and the Xe-lamp are shown in Figure 8.

539
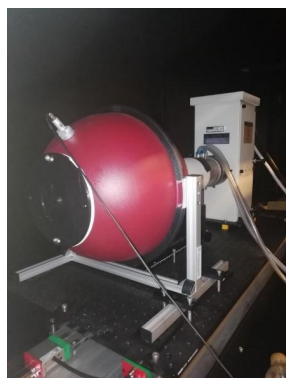


540
541 Figure 8. The integrating sphere with an interchangeable aperture and a monitor detector attached. The Xe-lamp housing
542 can be seen behind the sphere. Between the light source and the sphere there is a water filter and a lens imaging the arc
543 to the entrance of the sphere.

544

545 Collected data are used to derive the SVA of the POM following the method Boi et al. (1999). The solid viewing angle,
546 from the scanning centered at the origin of a local system of rectangular coordinates, is given by Eq. 11

547

$$\Delta\Omega = \iint_{\Delta A} \frac{E(x, y)}{E(0, 0)}\, \mathrm{d}x\mathrm{d}y \qquad \text{Eq. 11}$$

548 where E is the measured intensity (mA) and x and y (in radians) are the polar coordinates that determine the position of
549 the optical axis with respect to the position of the light source. The signals are registered as a function of the (x, y)
550 coordinates and a circular symmetry for the angular responsivity is assumed. Then a new system of coordinates centered
551 at the center of mass of the angular response is introduced and the needed parameters are obtained by fitting the
552 measurements.

553

554 The results are presented in Table 5, and in Figure 9 example of measurements are shown. The left figures display a 2D
555 heat map of the relative signal amplitude as a function of the two tilt angles. The fluctuations of the light source have
556 been taken into account by using correction coefficients obtained from the monitor detector data. The right figures present
557 the signal intensity as a 1D function of distance (r) from the center of mass. Measurements are particularly noisy, and it
558 is probably due to the use of an integrating sphere as source of light for a photometer, providing low radiation levels to
559 which the instrument has low sensitivity.

560

561 Table 5. SVA values and their uncertainties, obtained by laboratory calibrations and solar disk scanning methods
562

| | | SVA *e$^{-04}$ (1/sr) | | | | | | | Unc*e$^{-04}$ (1/sr) | | | | | | |
|---|---|---|---|---|---|---|---|---|---|---|---|---|---|---|---|
| | | 340 | 400 | 500 | 675 | 870 | 940 | 1020 | 340 | 400 | 500 | 675 | 870 | 940 | 1020 |
| POM_CNR AALTO | | 2.666 | 2.464 | 2.424 | 2.430 | 2.418 | 2.532 | 2.503 | / | / | / | / | / | / | / |
| POM_UV PMOD | | 2.198 | 2.298 | 2.302 | 2.343 | 2.396 | 2.433 | 2.382 | 0.016 | 0.011 | 0.009 | 0.012 | 0.012 | 0.009 | 0.011 |
| POM_CNR ROME | 3m | 2.4223 | 2.4633 | 2.4713 | 2.4588 | 2.5018 | 2.5038 | 2.5128 | 0.0144 | 0.0171 | 0.0190 | 0.0070 | 0.0056 | 0.0072 | 0.0090 |
| | 3n | 2.4363 | 2.4770 | 2.4825 | 2.4713 | 2.5255 | 2.5383 | 2.5425 | 0.0139 | 0.0171 | 0.0182 | 0.0071 | 0.0042 | 0.0063 | 0.0075 |
| POM_CNR IZANA | 3m | 2.3750 | 2.4370 | 2.4470 | 2.4382 | 2.4682 | 2.4882 | 2.4973 | 0.0680 | 0.0119 | 0.0084 | 0.0109 | 0.0507 | 0.0193 | 0.0196 |
| | 3n | 2.3813 | 2.4452 | 2.4538 | 2.4482 | 2.4798 | 2.5183 | 2.5258 | 0.0677 | 0.0122 | 0.0085 | 0.0124 | 0.0565 | 0.0196 | 0.0210 |
| POM_UV VALENCIA | 3m | 2.2528 | 2.3110 | 2.3368 | 2.3598 | 2.3923 | 2.4530 | 2.3910 | 0.0107 | 0.0143 | 0.0224 | 0.0222 | 0.0293 | 0.0197 | 0.0199 |
| | 3n | 2.2645 | 2.3180 | 2.3468 | 2.3708 | 2.4463 | 2.5040 | 2.4220 | 0.0090 | 0.0154 | 0.0222 | 0.0235 | 0.0309 | 0.0170 | 0.0217 |
| POM_UV ROME | 3m | 2.3080 | 2.3585 | 2.3625 | 2.3885 | 2.4770 | 2.5460 | 2.4720 | 0.0368 | 0.0092 | 0.0361 | 0.0396 | 0.0120 | 0.0410 | 0.0269 |
| | 3n | 2.2910 | 2.3475 | 2.3505 | 2.3770 | 2.4215 | 2.4940 | 2.4410 | 0.0438 | 0.0120 | 0.0389 | 0.0417 | 0.0170 | 0.0311 | 0.0240 |

563
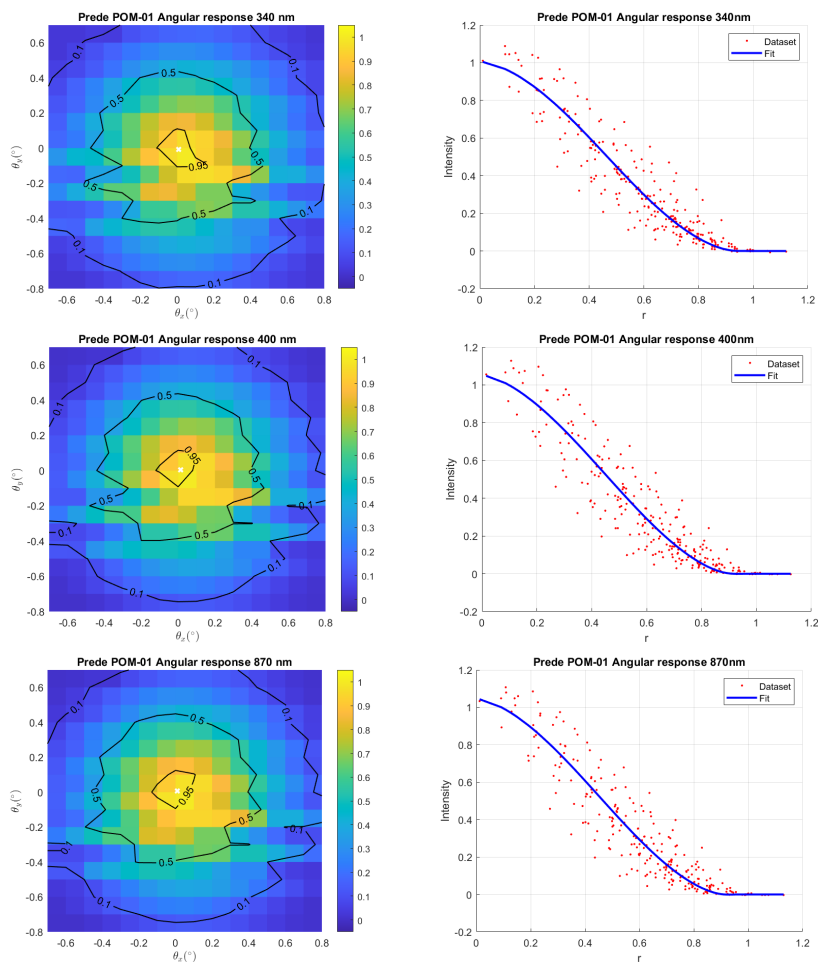564
565



566



567



568
569
570 Figure 9. Normalized angular responsivities for the POM_CNR. Heatmaps on the left have been normalised to the
571 maximum intensity. Graphs on the right have been normalised to the average intensity within r<0.19° where the
572 responsivities were assumed to forma a plateau.
573

### 4.2 Calibration at the laboratory of PMOD

574
575 The field of view characterisation facility at PMOD/WRC consists of a 250-kW Xe-Lamp source and a 2-axis goniometer
576 system with 0.2-mdeg resolution. The radiation from the Xe-Lamp shines on a Spectralon reflectance plate which
577 produces a lambertian radiation distribution. An aperture with diameter 12 mm is placed in front of the reflectance plate,
578 which is at a distance of 3600 mm from the goniometer system. Thus, the source has an apparent diameter of 0.19°. The
579 field of view measurement consists rotating the radiometer head in both axes from -1.1° to + 1.1° in steps of 0.04°. At
580 each position, the average of 10 measurements is stored, and every 100 positions, a reference measurement at the nominal
581 center position (0°, 0°) is performed to monitor the stability of the source and of the radiometer. A whole measurement
582 cycle for one channel of the radiometer takes 4.5 hours. The field of view (fov) of the instrument is obtained by
583 normalising the measurements at every angle with the reference signal at (0°,0°), obtained by interpolating the reference
584 measurements to the times of the individual measurements. For the measurements of this radiometer, the variability of
585 the reference measurements varied by 0.38% during the whole measurement cycle. The field of view measurement of the
586 Prede-POM_UV for the 500 nm channel is shown in Figure 10. As can be seen in the figure, the region with highest
587 responsivity above 99% of the maximum is circular, with a diameter of approximately 0.5°.
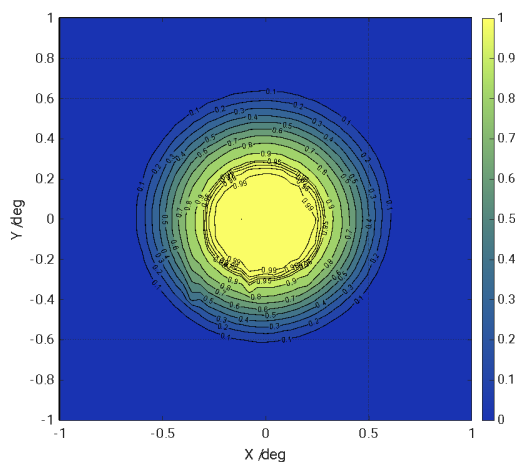


588
589 Figure 10: Field of view measurement at the 500 nm spectral channel of the Prede POM_UV. The measurements
590 were normalised to the maximum signal.

591
592 From these measurements, the solid view angle $\Omega$ of the radiometer at this spectral channel is obtained by Eq. 11.
593 The standard uncertainty of the solid angle measurements is obtained from the variability of the individual measurements,
594 combined with the variability of the system obtained from the monitoring signals as described above. For the Prede
595 POM_UV, the standard relative uncertainty of the solid angle determined from these measurements is 0.5%. Table 5
596 summarises the solid angle measurements determined for all spectral channels.

597
### 4.3 The solar disk methods

598
599
600 A methodology based on the scanning of the Solar disk, described in Boi et al. (1999) is used to determine SVA directly
601 from optical data. It consists of the scanning of the irradiance field around the Sun, centered at the origin of a local
602 system of a rectangular domain 2° by 2°; the irradiance is measured for all the channels at 21 x 21 gridded points around
603 the solar disk with an angular resolution 0.1° (Figure 11 a, b). The instrument automatically follows the sun during the
604 scanning, lasting several minutes, and measurements are corrected for the movement of the solar disk. The solid viewing
605 angle, from the scanning centered at the origin of a local system of rectangular coordinates, is given by Eq 11. An
606 elliptical system of coordinates centered at (0,0) is introduced and the needed parameters are obtained by fitting the
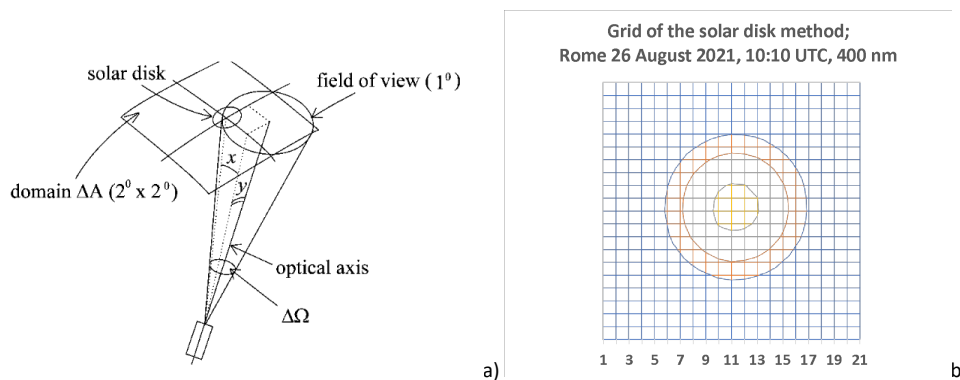607 measurements. This method is called solid3m hereafter.
608

609
610 Figure 11. Geometry of the solar disk scanning measurements (a) and 2D image of the scanning.
611

612 The field of view of a PREDE-POM is 1°, the size of the sun disk is about 0.5°, and the rectangular domain is 2°x2°,
613 therefore the data are taken from the sun for scattering angles up to 1.4° (= (1°) ×√2). As shown in Uchiyama et al.,
614 (2018) the influence of the direct solar irradiance as a light source extends up to 2.5°. To take this into consideration,
615 the integration of Eq 11 is performed by linear extrapolation for angles larger than 1.4°. Before starting the data
616 processing, the minimum measured value is subtracted from the measured values, then the values between 1.4 and 2.5°
617 are extrapolated.
618 The above-described method has been implemented by Uchiyama et al., (2018), (hereafter called solid3n) by not
619 subtracting the minimum value largely affecting the measurements of the scattering angle between 1 and 1.4° and
620 extrapolating the values between 1.4° and 2.5° using the data from 1.0° to 1.4°.
621 SVA was calculated with the two solid3m and solid3n methods, using measurements taken in Rome and Valencia for
622 the POM_UV and in Rome and Izana for the POM_CNR. The errors (ERR) for both 3m and 3n methods are estimated
623 as $((AM/ZM)-1)^2$ where AM is the measure and ZM is the calculated signals during the fitting phase. Only SVA having
624 ERR <0.2 is selected. The mean value over each campaign is assumed as the final SVA, and its std as the uncertainty
625 associated to the estimation. Results are in Table 5.
626 The behavior of SVA values along the time, for the two methods (dashed lines is 3m and solid lines is 3n) and the two
627 instruments, was also analyzed in order to evaluate the stability of the method (Figure 12). The coefficient of variation
628 for the temporal variation (Std/mean) ranges from 1.1 to 1.3% for the POM_UV and from 0.7 to 0.9% for the POM_CNR
629 with the exception of 340 nm (2.5%) and 870 (2.0%) due to the point of September 3 out of the general patter for 340
630 and 870 nm.
631
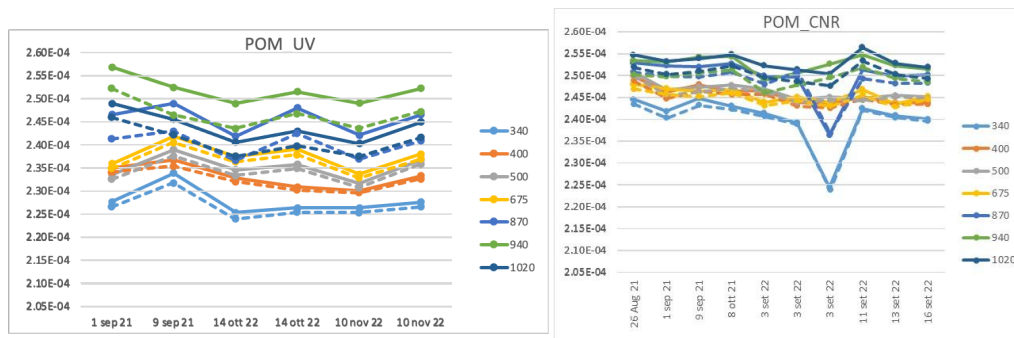


632
633
634 Figure 12: Temporal behaviour of SVA values [sr] from solid3m and 3n methods for POM_UV and POM_CNR co-
635 located in Rome.
636
637
638 **4.4 Comparisons**
639 SVA calculated with the two solid3m and solid3n methods, using measurements taken in Rome, Valencia, Davos and
640 Izana, are compared for both POM_UV and POM_CNR instruments against the laboratory calibrations performed in
641 AALTO and PMOD (Table 6 and Figure 13).
642

Atmospheric
Measurement
Techniques

Open Access

Discussions

$$Diff(\%) = \frac{(SVA - SVA^{lab})}{SVA^{lab}} \cdot 100$$

Eq.12

643 The solar disk scanning method uses the sun direct irradiance measurements as light source whereas the radiance from an
644 integrating sphere is the source at Aalto laboratory providing lower radiation levels and noisy measurements as already
645 mentioned in the paragraph 4.1. This is probably the reason why for the 340 nm channel of the POM_CNR, the
646 wavelength with the lowest intensity level, a large discrepancy is found ranging from 8.62% to 10.92% in Rome and
647 Izana.
648 The solar disk scanning in Rome and Izana analyzed with the solid3m method agrees generally better, with respect to
649 solid3n, with the laboratory calibration. The difference varies from a minimum of 0.03% at 400 nm to a maximum of
650 3.46% at 870 nm in Rome and from 0.23% at 1020 nm to 2.07% at 870 nm in Izana. Both the methods slightly
651 overestimate the SVA values in Rome. The 870 nm shows the highest discrepancy in both the sites and for both the
652 solid3m and 3n methods. At this moment we are not able to provide a reason for it, even if we expect it is due not to a
653 physical cause, but to an instrumental one. A general overestimation by the onsite procedures in the range [500-870] nm
654 wavelengths is observed in both the sites. The overestimation is explained considering that the field of view of a PREDE-
655 POM is 1° and the size of the sun disk is about 0.5°, therefore the scattered light from aerosols and air molecules is
656 included in the measurement of the direct solar irradiance. Moreover, the direct solar light strikes the lens and results in
657 "stray" light. The scattering contribution and stray light reaching the detector increase the output, and the integrated value
658 has a larger magnitude that can affect the estimation of the SVA. The overestimation is lower in Izana due to a less
659 important scattering effect.
660 For the POM_UV, as for the other one, the 340 nm wavelength has a larger disagreement respect to the other wavelengths
661 reaching values of 4 and 5 % for both the sun disk methods, not explainable at this state of the art. Both in Rome and
662 Valencia a generally better accordance with the laboratory calibration is for the solim3m method when in the range [400-
663 870] nm the difference is below 1.5% and 2.15% in Valencia and Rome, respectively. For the 1020 nm the comparison
664 in Rome has a larger difference up to 2.63%. Also for this POM a general overestimation of SVA from onsite calibration
665 is visible in Rome, as explained in the above paragraph.
666 Finally, we compared the performance of the on-site calibration procedure, method 3m, in Rome for the two co-located
667 instruments calibrated at the two different laboratories (Figure 14). The SVA values for POM_CNR better agree with the
668 calibration performed in AALTO laboratory, with the exception of 340 nm and 870 nm.
669

| | Wl [nm] | (%) diff s3m-s3n | (%) diff lab-3m | (%) diff lab-3n | | Wl [nm] | (%) diff s3m-s3n | (%) diff lab-3m | (%) diff lab-3n |
|---|---|---|---|---|---|---|---|---|---|
| | **AALTO calibration (lab)** | | | | | **PMOD calibration (lab)** | | | |
| POM_CNR ROME | 340 | -0.58 | 9.14 | 8.62 | POM_UV VALENCIA | 340 | -0.52 | -2.49 | -3.03 |
| | 400 | -0.56 | 0.03 | -0.53 | | 400 | -0.30 | -0.57 | -0.87 |
| | 500 | -0.46 | -1.95 | -2.41 | | 500 | -0.43 | -1.51 | -1.94 |
| | 675 | -0.51 | -1.18 | -1.70 | | 675 | -0.47 | -0.71 | -1.18 |
| | 870 | -0.95 | -3.46 | -4.45 | | 870 | -2.26 | 0.16 | -2.10 |
| | 940 | -1.38 | 1.12 | -0.25 | | 940 | -2.08 | -0.82 | -2.92 |
| | 1020 | -1.18 | -0.39 | -1.58 | | 1020 | -1.30 | -0.38 | -1.68 |
| POM_CNR IZANA | 340 | -0.27 | 10.92 | 10.68 | POM_UV ROME | 340 | -0.74 | -4.23 | -5.00 |
| | 400 | -0.34 | 1.10 | 0.76 | | 400 | -0.47 | -2.15 | -2.63 |
| | 500 | -0.28 | -0.95 | -1.23 | | 500 | -0.51 | -2.11 | -2.63 |
| | 675 | -0.41 | -0.34 | -0.75 | | 675 | -0.48 | -1.45 | -1.94 |
| | 870 | -0.47 | -2.07 | -2.56 | | 870 | -2.29 | -1.06 | -3.38 |
| | 940 | -1.21 | 1.73 | 0.54 | | 940 | -2.09 | -2.51 | -4.64 |
| | 1020 | -1.14 | 0.23 | -0.91 | | 1020 | -1.27 | -2.48 | -3.78 |

670
671
672 Table 6: Differences between SVA values from the onsite calibration methods and the laboratory calibrations for the two
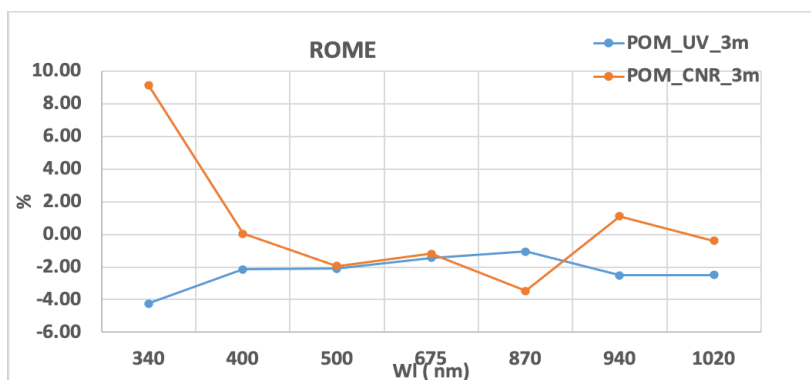673 POMs.
674

675
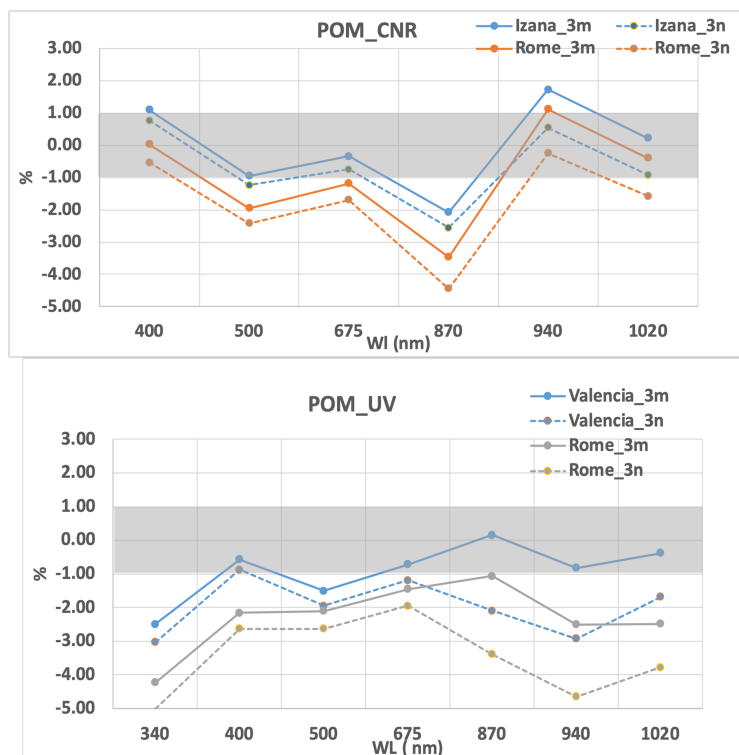
676
677    Figure 13:  % difference of SVA values from sun disk methods and laboratory calibrations for POM_CNR (top) and
678       POM_UV (bottom).
679



680
681    Figure 14: difference of SVA values from sun disk method 3m and laboratory calibrations for POM_CNR (orange) and
682                            POM_UV (blue) co-located in Rome.
683
684
685    **5. Conclusions**
686
687    The performance of the on-site calibration procedures applied to two PREDE-POMs instruments, was evaluated using
688    intercomparison campaigns and laboratory calibrations. Two periods were chosen for the validation: a) from September
689    2021 to November 2022, where 6 different calibration methodologies were compared against the SL method performed
690    in Izana in September 2022; the reference SL calibration was done in September 2022 and there is no availability of a
691    monthly reference calibration in the previous 12 months, to watch the stability of the instruments and check if their
692    shipments or usage affected the calibrations;  b) from August 2017 to September 2021, where the calibration transfer
693    from a PFR during the QUATRAM campaigns was used to evaluate the on-site methodologies.

694　The comparison against the SL showed an agreement generally improving with the wavelengths but with a small
695　worsening at 1020 nm. The IL works better in Davos with an agreement below 0.5% except at 1020 nm where it increases
696　up to about 1.5%. A very good accordance is also found in Valencia in November 2022, always within 0.8% except at
697　500 and 675 nm (within 1.5%). The similarity between the two cases is probably due to the very low turbidity recorded
698　in this month in Valencia, that makes the atmosphere optically more similar to the one in Davos. These results are in
699　accordance with Nakajima et al., (2021) where the estimation of the retrieval accuracy of $V_0$ from IL gives values of about
700　2.4% in Rome and around 0.3% - 0.5% at the mountain sites of Mt. Saraswati and Davos. These values are consistent
701　with the RMSD in the aerosol optical depth comparisons with other networks, that is less than 0.02 for $\lambda \geq 500$ nm and
702　about 0.03 for shorter wavelengths in city areas; smaller values of less than 0.01 are found in mountain comparisons.
703　The XIL provides a consistent improvement (with values within 1%) only in Rome for all the wavelengths, but in very
704　clean atmosphere as in Davos it was not possible to retrieve values at 1020 nm.
705　The 340 nm is the wavelength with the most problematic results for the on-site procedures in Rome (differences around
706　4%) probably because of the molecular polarization that causes calibration errors from IL and XIL methods at the UV
707　region (340 nm), especially in low aerosol loading atmosphere.
708　In Rome the calibrations transferred from PFR in September 2021 differ against the SL (performed in September 2022)
709　in the range [-2.1%; -1.9%] at 500 nm for the two POMs, and the difference with the transfer from Cimel is about -1.6%.
710　However simultaneous calculation of $V_0$ in September 2021 with IL and XIL at 500 nm provides values that differ from
711　the SL of less then 0.5% for POM_CNR and 1.2% from POM_UV. The reason of such discrepancy must be studied,
712　because is not attributable to a change in the equipment due to shipping or usage, since it would have been visible also
713　from the on-site methodologies.
714　For both the POMs the comparison with PTB laboratory calibration shows very high underestimations (down to -10%
715　except for POM_CNR, and -8% for POM_UV). The discrepancies between the laboratory-based values and the field
716　measurements are probably due to different operating conditions of the instruments (e.g., different alignment and
717　measurement geometries, operating modes, polarization, etc.) and unknown POM settings (e.g., POM temperatures,
718　signal readout procedures) under which the instruments were calibrated in the laboratory and used in the field.
719　The long term comparison of the on-site methods with the calibration transfer from PFR was performed in Davos and
720　Rome, and showed  for IL differences always greater than the uncertainties (%CV) of the method, for both wavelengths,
721　with the exception of Davos in 2017. Values are around 1% in Davos whereas the largest differences are in Rome and at
722　500 nm, likely due to the unfulfilled assumption that the refractive index do not largely change during the Langley plot.
723　O the other hand for XIL many differences are within the uncertainties (%CV) of the method, and those higher are closer
724　to the %CV values than in the IL method. XIL improves the agreement particularly in Rome where the largest difference
725　reduces from 3.5% to 2.5% at 500 nm and from 3% to 1.7% at 870 nm.
726　Future studies are planned to understand the effects of atmospheric scattering variability on the IL method and of the
727　molecular polarization on 340 nm, switching from the use of the Skyrad 4.2 pack to the Skyrad_MRI (Kudo et al.,2021).
728　A more close look at the effects on AOD is also underway on a second paper.
729

730　The solar disk scanning methods 3m and 3n performed in Rome and Izana were compared against the laboratory
731　calibrations. The difference varied from a minimum of 0.03% at 400 nm to a maximum of 3.46% at 870 nm in Rome and
732　from 0.23% at 1020 nm to 2.07% at 870 nm in Izana. Both the methods slightly overestimate the SVA values in Rome.
733　The 870 nm shows the highest discrepancy in both the sites and for both the solid3m and 3n methods for the two POMs.
734　A generally better accordance with the laboratory calibration was found for the solim3m method. An overestimation by
735　the on-site procedures in the range [500-870] nm wavelengths is observed in both the sites due probably to an effect of
736　the scattered light from aerosols and air molecules included in the measurement and to a contribution of the direct solar
737　light striking the lens. The scattering contribution and stray light reaching the detector increase the output, and the
738　integrated value has a larger magnitude that can affect the estimation of the SVA. The overestimation was lower in Izana
739　due to a less important scattering effect.

740　**Acronyms tables**

| ACTRIS | Aerosol, Clouds and Trace Gases Research Infrastructure |
|--------|--------------------------------------------------------|
| AM | Measured signal during solar disk scan |
| AOD | Aerosol Optical Depth |
| CIMO | Commission for Instruments and Methods of Observation |
| CV | Coefficient of Variation |
| DN | Digital Signals |
| DUT | Detector Under Test |
| DVM | Digital Voltage Meter |
| ERR | Errors |
| FOV | Field Of View |
| FRC | Filter Radiometer Comparison |
| FWHM | Full Width at Half Maximum |

Atmospheric
Measurement
Techniques
Discussions

Open Access

EGU

| GAW | Global Atmospheric Watch |
|---|---|
| I/U | Current-To-Voltage Converter |
| IL | Improved Langley Method |
| LCD | Liquid Crystal Display |
| LSA | Laser Spectrum Analyzer |
| MAPP | Metrology for Aerosol optical Properties |
| MFRSR | Multifilter Rotating Shadowband Radiometer |
| MRI | Meteorological Research Institute |
| MUX | Multiplexer |
| NDF | Neutral-Density Filter |
| NIST | National Institute of Standards and Technology |
| OPO | Optical Parametric Oscillator |
| PFR | Precision Filter Radiometer |
| PMOD | Physikalisch-Meteorologische Observatorium Davos |
| POM_CNR | POM radiometer of Consiglio Nazionale delle Ricerche |
| POM_UV | POM radiometer of Univeristy of Valencia |
| PTB | Physikalisch-Technische Bundesanstalt laboratory |
| QUATRAM | QUALity and TRaceabiliy of Atmospheric aerosol Measurements |
| REF | Reference |
| RMSD | Root Mean Square Deviation |
| SHG | Second Harmonic module |
| SL | Standard Langley method |
| STD | Standard Deviation |
| SVA | Solid View Angle |
| THG | Third Harmonic module |
| TULIP | TUable Lasers In Photometry |
| UV | Ultra Violet |
| VIS | Visible |
| WMO | World Meteorological Organization |
| WORCC | World optical depth research and calibration center |
| XIL | Cross Improved Langley method |
| ZM | calculated signals during the fitting phase in the solar disk scan |

741

**Competing interests**

At least one of the (co-)authors is a member of the editorial board of Atmospheric Measurement Techniques. Monica Campanelli and Stelios Kazadzis are co-editors of the Skynet Special issue.

**References**

Aeronet webpage: https://aeronet.gsfc.nasa.gov/new_web/Documents/Inversion_products_for_V3.pdf.

Boi P., Glauco Tonna, Giuseppe Dalu, Teruyuki Nakajima, Bruno Olivieri, Alberto Pompei, Monica Campanelli, and R. Rao, "Calibration and data elaboration procedure for sky irradiance measurements," Appl. Optics,38, 896–907, https://doi.org/10.1364/AO.38.000896, 1999.

Campanelli M., Teruyuki Nakajima, and Bruno Olivieri, "Determination of the solar calibration constant for a sun-sky radiometer: proposal of an in-situ procedure," Appl. Opt. 43, 651-659 (2004)

Atmospheric
Measurement
Techniques
Discussions

765   Campanelli M., Víctor Estellés, Claudio Tomasi, Teruyuki Nakajima, Vincenzo Malvestuto, and José Antonio Martínez-
766   Lozano, "Application of the SKYRAD Improved Langley plot method for the in situ calibration of CIMEL Sun-sky
767   photometers," Appl. Opt. 46, 2688-2702 (2007)
768
769   Campanelli M., A.M. Iannarelli , S. Kazadzis, N. Kouremeti, S. Vergari, V.Estelles, H. Diemoz, A. di Sarra, A. Cede:
770   "The QUATRAM Campaign: QUAlity and TRaceabiliy of Atmospheric aerosol Measurements". Instruments and
771   Observing Methods; Report No. 132; The 2018 WMO/CIMO Technical Conference on Meteorological and
772   Environmental Instruments and Methods of Observation (CIMO TECO-2018) "Towards fit-for-purpose environmental
773   measurements" 8 - 11 October 2018, Amsterdam, the Netherlands.
774
775   Coddington, O. M., Richard, E. C., Harber, D., Pilewskie, P., Woods, T. N., Snow, M., et al. (2023). Version 2 of the
776   TSIS-1 Hybrid Solar Reference Spectrum and Extension to the Full Spectrum. Earth and Space Science, 10,
777   e2022EA002637. https://doi.org/10.1029/2022EA002637
778
779   Cuevas, E., Milford, C., Barreto, A., Bustos, J. J., García, O. E., García, R. D., Marrero, C., Prats, N., Ramos, R.,
780   Redondas, A., Reyes, E., Rivas-Soriano, P. P., Romero-Campos, P. M., Torres, C. J., Schneider, M., Yela, M., Belmonte,
781   J., Almansa, F., López-Solano, C., Basart, S., Werner, E., Rodríguez, S., Afonso, S., Alcántara, A., Álvarez, O., Bayo,
782   C., Berjón, A., Carreño, V., Castro, N. J., Chinea, N., Cruz, A. M., Damas, M., Gómez-Trueba, V., González, Y., Guirado-
783   Fuentes, C., Hernández, C., León-Luís, S. F., López-Fernández, R., López-Solano, J., Parra, F., Pérez de la Puerta, J.,
784   Rodríguez-Valido, M., Sálamo, C., Santana, D., Santo-Tomás, F., Sepúlveda, E., and Serrano, A.: Izaña Atmospheric
785   Research Center Activity Report 2019–2020, (Eds. Cuevas, E., Milford, C. and Tarasova, O.), State Meteorological
786   Agency (AEMET), Madrid, Spain and World Meteorological Organization, Geneva, Switzerland, NIPO: 666-22-014-0,
787   WMO/GAW Report No. 276, https://doi.org/10.31978/666-22-014-0, 2022.
788
789   Estelle´s, V., et al. (2004), Aerosol related parameters intercomparison of Cimel sunphotometers in the frame of the
790   VELETA 2002 field campaign, Opt. Pura Apl., 37(3), 3289 – 3297
791
792   Giles, D. M., Sinyuk, A., Sorokin, M. G., Schafer, J. S., Smirnov, A., Slutsker, I., Eck, T. F., Holben, B. N., Lewis, J. R.,
793   Campbell, J. R., Welton, E. J., Korkin, S. V., and Lyapustin, A. I.: Advancements in the Aerosol Robotic Network
794   (AERONET) Version 3 database – automated near-real-time quality control algorithm with improved cloud screening for
795   Sun photometer aerosol optical depth (AOD) measurements, Atmos. Meas. Tech., 12, 169–209,
796   https://doi.org/10.5194/amt-12-169-2019, 2019.
797
798   Gröbner, J., Kouremeti, N., Hülsen, G., Zuber, R., Ribnitzky, M., Nevas, S., Sperfeld, P., Schwind, K., Schneider, P.,
799   Kazadzis, S., Barreto, Á., Gardiner, T., Mottungan, K., Medland, D., and Coleman, M.: Spectral aerosol optical depth
800   from SI-traceable spectral solar irradiance measurements, Atmos. Meas. Tech., 16, 4667–4680,
801   https://doi.org/10.5194/amt-16-4667-2023, 2023
802
803   Holben, B.N., et al., 1998. AERONET—A federated instrument network and data archive for aerosol characterization.
804   Remote Sens. Environ. 66, 1–16. https://doi. org/10.1016/S0034-4257(98)00031-5.
805
806   Holben, B. N., T. F. Eck, I. Slutsker, A. Smirnov, A Sinyuk, J. Schafer, D. Giles, O. Dubovik, 2006: Aeronet's Version
807   2.0 quality assurance criteria, Proc. SPIE 6408, Remote Sensing of the Atmosphere and Clouds, 64080Q,
808   doi:10.1117/12.706524 )
809   Kazadzis, S., Kouremeti, N., Diémoz, H., Gröbner, J., Forgan, B. W., Campanelli, M., Estellés, V., Lantz, K., Michalsky,
810   J., Carlund, T., Cuevas, E., Toledano, C., Becker, R., Nyeki, S., Kosmopoulos, P. G., Tatsiankou, V., Vuilleumier, L.,
811   Denn, F. M., Ohkawara, N., Ijima, O., Goloub, P., Raptis, P. I., Milner, M., Behrens, K., Barreto, A., Martucci, G., Hall,
812   E., Wendell, J., Fabbri, B. E., and Wehrli, C.: Results from the Fourth WMO Filter Radiometer Comparison for aerosol
813   optical depth measurements, Atmos. Chem. Phys., 18, 3185–3201, https://doi.org/10.5194/acp-18-3185-2018, 2018a.
814   Kazadzis, S., Kouremeti, N., Nyeki, S., Gröbner, J., and Wehrli, C.: The World Optical Depth Research and Calibration
815   Center (WORCC) quality assurance and quality control of GAW-PFR AOD measurements, Geosci. Instrum. Method.
816   Data Syst., 7, 39–53, https://doi.org/10.5194/gi-7-39-2018, 2018b.
817   Kim, S.-W., Yoon, S.-C., Dutton, E., Kim, J., and Wehrli, C.and Holben, B.: Global surface-based sun photometer
818   network for long-term observations of column aerosol optical properties: intercomparison of aerosol optical depth,
819   Aerosol Sci. Tech., 42, 1–9, https://doi.org/10.1080/02786820701699743, 2008
820
821   Kudo, R., Diémoz, H., Estellés, V., Campanelli, M., Momoi, M., Marenco, F., Ryder, C. L., Ijima, O., Uchiyama, A.,
822   Nakashima, K., Yamazaki, A., Nagasawa, R., Ohkawara, N., and Ishida, H.: Optimal use of the Prede POM sky

radiometer for aerosol, water vapor, and ozone retrievals, Atmos. Meas. Tech., 14, 3395–3426, https://doi.org/10.5194/amt-14-3395-2021, 2021.

Application of the SKYRAD Improved Langley plot method for the in situ calibration of CIMEL Sun-sky photometers, M Campanelli, et al., Applied optics 46 (14), 2688-2702, 2007

Momoi, M., 2022: Development of the efficient calculation of polarized radiative transfer based on the correlated k-distribution method and forward peak truncation approximation (Doctoral dissertation, Chiba University, Japan), retrieved from https://opac.ll.chiba-u.jp/da/curator/900120935/

Nakajima, T., Tonna, G., Rao, R., Kaufman, Y., and Holben, B.: Use of sky brightness measurements from ground for remote sens- ing of particulate polydispersions, Appl. Optics, 35, 2672–2686, https://doi.org/10.1364/AO.35.002672, 1996.

Nakajima, T., Campanelli, M., Che, H., Estellés, V., Irie, H., Kim, S.-W., Kim, J., Liu, D., Nishizawa, T., Pandithurai, G., Soni, V. K., Thana, B., Tugjsurn, N.-U., Aoki, K., Go, S., Hashimoto, M., Higurashi, A., Kazadzis, S., Khatri, P., Kouremeti, N., Kudo, R., Marenco, F., Momoi, M., Ningombam, S. S., Ry- der, C. L., Uchiyama, A., and Yamazaki, A.: An overview of and issues with sky radiometer technology and SKYNET, At- mos. Meas. Tech., 13, 4195–4218, https://doi.org/10.5194/amt- 13-4195-2020, 2020.
Ningombamet SS et al Calibration of a Sky radiometer (Prede) using observations obtained from Hanle and Merak high-altitude stations in Ladakh,., Atmospheric research 143, 118-128, 2014

Shaw G. E., "Error analysis of multi-wavelength sun photome- try," Pure Appl. Geophys. 114, 1–4 (1976).

Tanaka, M., Takamura, T., Nakajima, T., Refractive Index and Size Distribution of Aerosols as Estimated from Light Scattering Measurements, Journal of Climate and Applied Meteorology, 22, 1253-1261, 1983. https://doi.org/10.1175/1520-0450(1983)022<1253:RIASDO>2.0.CO;2

Tonna G., T. Nakajima, and R. Rao, "Aerosol features retrieved from solar aureole data: a simulation study concerning a turbid atmosphere," Appl. Opt. 34, 4486-4499 (1995)

Toledano, C., González, R., Fuertes, D., Cuevas, E., Eck, T. F., Kazadzis, S., Kouremeti, N., Gröbner, J., Goloub, P., Blarel, L., Román, R., Barreto, Á., Berjón, A., Holben, B. N., and Cachorro, V. E.: Assessment of Sun photometer Langley calibration at the high-elevation sites Mauna Loa and Izaña, Atmos. Chem. Phys., 18, 14555–14567, https://doi.org/10.5194/acp-18-14555-2018, 2018.

Torres, B., Toledano, C., Berjón, A., Fuertes, D., Molina, V., Gonzalez, R., Canini, M., Cachorro, V. E., Goloub, P., Podvin, T., Blarel, L., Dubovik, O., Bennouna, Y., and de Frutos, A. M.: Measurements on pointing error and field of view of Cimel-318 Sun photometers in the scope of AERONET, Atmospheric Measurement Techniques, 6, 2207–2220, https://doi.org/10.5194/amt-6-2207-2013, 2013.

Uchiyama, A., Matsunaga, T., and Yamazaki, A.: The instrument constant of sky radiometers (POM-02) – Part 2: Solid view angle, Atmos. Meas. Tech., 11, 5389–5402, https://doi.org/10.5194/amt-11-5389-2018, 2018.

Young H. D., Statistical Treatment of Experimental Data (McGraw-Hill, 1962), pp. 78–80.)

WMO: WMO/GAW Experts Workshop on a Global Surface-Based Network for Long Term Observations of Column Aerosol Optical Properties, GAW Report No. 162, WMO TD No. 1287, available at: https://library.wmo.int/index.php?lvl=notice_display&id=11094 (last access: 12 June 2023), 2005.

WMO: Abridged final report with resolutions and recommendations, GAW Report WMO TD No. 1019, WMO-CIMO Fourteenth session Geneva 7–14 December 2006, https://library.wmo.int/index.php?lvl=notice_display&id=9912, (last access: 12 June 2023), 2007.

WMO, Stelios Kazadzis, Natalia Kouremeti, Julian Gröbner Fifth WMO Filter Radiometer Comparison (FRC-V) 27 September to 25 October 2021 Davos, Switzerland (GAW report 280),https://library.wmo.int/index.php?lvl=notice_display&id=22267 (last access: 12 June 2023), 2023.